Query Details

Back to Main Page

1. Since the references were not cited in numerical order, they have been renumbered in the order of appearance. Please check.

2. Please check your article carefully, coordinate with any co-authors and enter all final edits clearly in the eproof, remembering to save frequently. Once corrections are submitted, we cannot routinely make further changes to the article.

3. Note that the eproof should be amended in only one browser window at any one time; otherwise changes will be overwritten.

4. Author surnames have been highlighted. Please check these carefully and adjust if the first name or surname is marked up incorrectly, as this will affect indexing of your article in public repositories such as PubMed. Also, carefully check the spelling and numbering of all author names and affiliations, and the corresponding author(s) email address(es). Please note that email addresses should only be included for designated corresponding authors, and you cannot change corresponding authors at this stage except to correct errors made during typesetting.

5. You cannot alter accepted Supplementary Information files except for critical changes to scientific content. If you do resupply any files, please also provide a brief (but complete) list of changes. If these are not considered scientific changes, any altered Supplementary files will not be used, only the originally accepted version will be published.

6. Please note we reserve significant and its derivative for statistical significance. Please reword where this not the intended meaning.

7. Please check that there has been no corruption of mathematical symbols. Only single-letter variables are set in italics (but not their subscripts unless these are also variables); multi-letter variables are set in roman. Vectors are set as bold and upright; matrices are set as italic only. We set capital Greek letters in italics if they are variables. We set i, Euler's number (e) and pi upright. Please check that the maths has been formatted correctly according to this style

8. Please add the definition for ‘FL’ in the abbreviations.

9. If ref. 7 (preprint) has now been published in final peer-reviewed form, please update the reference details if appropriate.

10. If ref. 32 (preprint) has now been published in final peer-reviewed form, please update the reference details if appropriate.

11. If ref. 49 (preprint) has now been published in final peer-reviewed form, please update the reference details if appropriate.

12. Please provide page range for refs. 92, 118.

13. Please provide the year of publication for references 59,94.

14. Please provide the year of publication for reference 109.

15. If ref. 148 (preprint) has now been published in final peer-reviewed form, please update the reference details if appropriate.

16. If ref. 162 (preprint) has now been published in final peer-reviewed form, please update the reference details if appropriate.

17. If ref. 168 (preprint) has now been published in final peer-reviewed form, please update the reference details if appropriate.

18. Please provide more information for ref. 180.

19. If ref. 212 (preprint) has now been published in final peer-reviewed form, please update the reference details if appropriate.

Primer

Loading web-font TeX/Caligraphic/Regular

Holotomography

Geon Kim Affiliationids : Aff1 Aff2
Herve Hugonnet Affiliationids : Aff1 Aff2
Kyoohyun Kim Affiliationids : Aff3
Jae-Hyuk Lee Affiliationids : Aff4
Sung Sik Lee Affiliationids : Aff5 Aff6
Jeongmin Ha Affiliationids : Aff7
Chungha Lee Affiliationids : Aff1 Aff2
Hoewon Park Affiliationids : Aff8
Ki-Jun Yoon Affiliationids : Aff8
Yongdae Shin Affiliationids : Aff9
Gabor Csucs Affiliationids : Aff6
Ian Hitchcock Affiliationids : Aff10
Luke Mackinder Affiliationids : Aff10
Ji Hyang Kim Affiliationids : Aff11
Tae Hyun Hwang Affiliationids : Aff12
Seongsoo Lee Affiliationids : Aff4 Aff13
Peter O'Toole Affiliationids : Aff10
Bon-Kyoung Koo Affiliationids : Aff7
Jochen Guck Affiliationids : Aff3
YongKeun Park✉
Email : yk.park@kaist.ac.kr
Affiliationids : Aff1 Aff2 Aff14, Correspondingaffiliationid : Aff1

Aff1 Department of Physics, Korea Advanced Institute of Science and Technology (KAIST), Daejeon, Republic of Korea

Aff2 KAIST Institute for Health Science and Technology, Daejeon, Republic of Korea

Aff3 Max Planck Institute for the Science of Light and Max-Planck-Zentrum für Physik und Medizin, Erlangen, Germany

Aff4 Gwangju Centre, Korea Basic Science Institute, Gwangju, Republic of Korea

Aff5 Department of Biology, Institute of Biochemistry, ETH Zurich, Zurich, Switzerland

Aff6 Scientific Center for Optical and Electron Microscopy, ETH Zurich, Zurich, Switzerland

Aff7 Center for Genome Engineering, Institute for Basic Science, Daejeon, Republic of Korea

Aff8 Department of Biological Sciences, KAIST, Daejeon, Republic of Korea

Aff9 Department of Mechanical Engineering, Seoul National University, Seoul, Republic of Korea

Aff10 Department of Biology, University of York, Heslington, York, UK

Aff11 Department of Obstetrics and Gynecology, Fertility Centre of CHA Bundang Medical Centre, CHA University School of Medicine, Seongnam, Republic of Korea

Aff12 Mayo Clinic Florida, Jacksonville, FL, USA

Aff13 Department of Systems Biotechnology, Chung-Ang University, Anseong-si, Gyeonggi-do, Republic of Korea

Aff14 Tomocube Inc., Daejeon, Republic of Korea

Abstract

Holotomography (HT) represents a 3D, label-free optical imaging methodology that leverages refractive index as an inherent quantitative contrast for imaging. This technique has recently seen significant advancements, creating novel opportunities for the comprehensive visualization and analysis of living cells and their subcellular organelles. It has manifested wide-ranging applications spanning cell biology, biophysics, microbiology and biotechnology, substantiating its vast potential. In this Primer, we elucidate the fundamental physical principles underpinning HT, detailing its experimental implementations and providing case studies of

representative research employing this methodology. We also venture into interdisciplinary territories, exploring how HT harmonizes with emergent technologies, such as regenerative medicine, 3D biology and organoid-based drug discovery and screening. Looking ahead, we engage in a prospective analysis of potential future trajectories for HT, discussing innovation-focused initiatives that may further elevate this field. We also propose possible future applications of HT, identifying opportunities for its integration into diverse realms of scientific research and technological development.

Editor's Summary

Holotomography is a 3D, label-free optical imaging method for visualizing living tissues and cells. In this Primer, Kim et al. discuss the implementation of holotomography in various applications ranging from cell biology to biophysics and biotechnology.

Introduction

The examination and analysis of cells AQ1 are integral to understanding their complex nature, diagnosing diseases and facilitating the creation of innovative drugs. Over time, a multitude of microscopy technologies have been devised for cellular observation, starting with the optical microscope in the 1750s. Since then, a myriad of microscopy techniques have been refined, paving the way for observing and comprehending various life phenomena that were hitherto unseen[1]. This progress has considerably enriched our understanding of biology and medical knowledge, liberating humanity from a range of diseases. AQ2 AQ3 AQ4 AQ5

Contemporary research underscores the necessity for extended observation of living cells, thereby revealing the constraints of traditional microscopy techniques. A great challenge when imaging biological samples is their transparency, which results in poor contrast. Phase-contrast microscopy solves this problem by visualizing the delay in light propagation caused by the sample. However, it provides only qualitative contour data in a 2D plane, lacking precise 3D information or quantitative data on cell mass and volume. Fluorescence microscopy offers subcellular molecular imaging, yet prerequisites such as fixation may alter cells or compromise their innate properties, and prolonged observation is impeded by phototoxicity and photobleaching from fluorescence[2]. These limitations accentuate the potential of label-free imaging[3]. Quantitative phase imaging (QPI) — which includes holotomography (HT), among the growing label-free imaging fields — is a promising technique owing to its high resolution, imaging speed and wide availability[4]. QPI is a field of imaging that accounts for both the intensity and phase of light. HT, as a subset of QPI[5], reconstructs the 3D refractive index (RI) of a sample, accounting for the complex optical field scattered from the sample (Fig. 1). This scattering takes place regardless of sample labelling or staining, thus providing a quantitative physical profile. As a result, HT overcomes the limitations of traditional microscopy methodologies such as phase contrast and fluorescence microscopy, which provide limited morphological and structural information on the sample.

Fig. 1

An overview of holotomography and diverse implementations.

a, Similarities drawn between CT and HT. **b**, As a subset of QPI, HT reconstructs the 3D RI of a sample without using exogenous labelling agents. **c**, Coherent HT leverages light scattering from coherent plane-wave illumination, as an extension of QPI techniques. **d**, Temporally low-coherence HT adopts a low-coherence source to curtail noise. **e**, Spatially low-coherence HT diminishes optical hardware prerequisites. DIC, differential interference contrast; QPI, quantitative phase imaging; RI, refractive index.

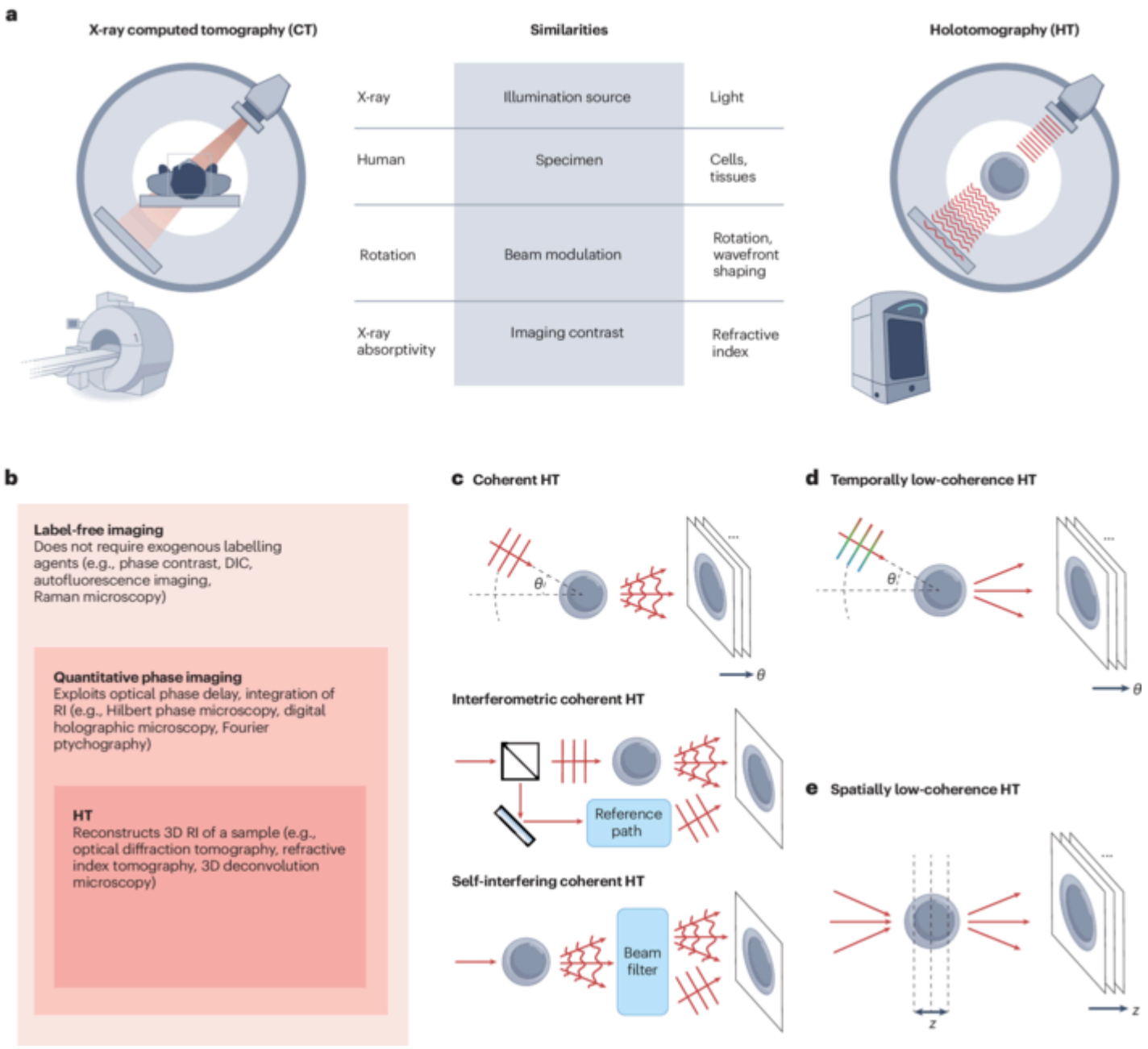

HT renders precise measurements of the 3D RI distribution of transparent specimens, such as biological cells, with superior spatial resolution and contrast. The technology builds upon the principles of computed tomography (CT) but substitutes X-rays with light to reconstruct the RI distribution of the sample (Fig. 1a). In CT, X-rays are used to reconstruct a 3D image of a target object based on the absorption of X-rays by different tissues. Similarly, HT uses light instead of X-rays to reconstruct the RI distribution. This technique involves capturing a series of 2D optical images of a specimen under various illumination modulations. Each optical image contains phase and amplitude information, resulting from the interference of light with the specimen. HT algorithms then integrate these multiple 2D images to reconstruct a 3D RI map of the sample, revealing internal structures without the need for external labels or dyes.

Although HT imaging can carry out a wide variety of realizations, HT is categorized based on the illumination strategy being used: coherent, temporally low-coherence and spatially low-coherence. Coherent HT involves recording the transmitted field under various illumination angles through interference. Temporally low-coherence HT operates in a similar manner, in which light source is temporally slightly incoherent. By contrast, spatially low-coherence HT records the transmitted intensity under spatially incoherent illumination at different depths inside the sample.

HT has extensive applications in biological research[5] (Fig. 2), encompassing cell biology, biophysics, neuroscience, immunology and cancer research. The suite of advantages provided by HT — that it is non-invasive, volumetric and provides sustainable imaging — makes it ideal for use in biomedical investigations. The labour-intensive and often sample-altering preparations of traditional microscopy methods are bypassed with HT to enable the study of live cells and potentially aid in therapeutic interventions. Its 3D imaging capability spans realms such as 3D cultures, organoids[6, 7], tissue engineering[8], microfluidics[9, 10, 11], organ-on-a-chip systems[12] and 3D bioprinting[13], whereas its sustained time-lapse measurement also allows continuous assessment[7, 14] of long-term phenomena.

Fig. 2

General landscape of contemporary holotomography applications.

Applications of holotomography (HT) extend to a range of scales, both spatial and temporal. The spatial scale ranges from micrometre-scale single cells to millimetre-scale tissues. Major examples of single cells studied with HT include microorganisms and blood cells that provide pathological insights. Larger cells have been studied concerning the subcellular structures — such as lipid droplets — and their dynamics. Multicellular subjects of HT include tissues, stem cell colonies, organoids and embryos. Although studying tissues accompanies covering the largest spatial scale, others also focus on the temporal dynamics.

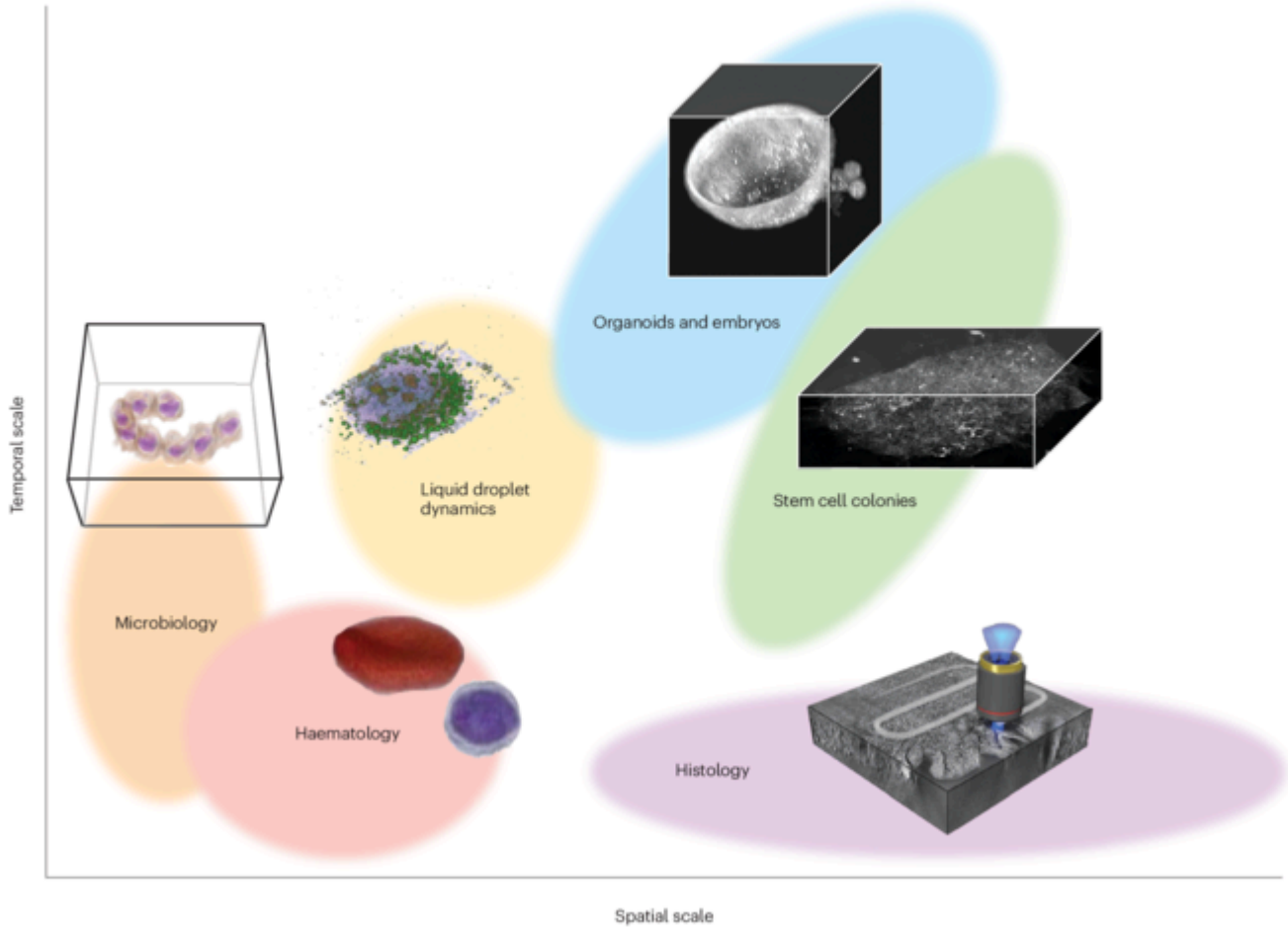

HT can be integrated with other imaging modalities, such as fluorescence microscopy and Raman spectroscopy, to provide supplementary information on the chemical and structural properties of samples. In recent years, HT has been commercialized by start-up companies, growing increasingly accessible in research laboratories, hospitals and biotechnology companies. The rising popularity and availability of this technology are anticipated to catalyse the development of new diagnostic and therapeutic tools for various diseases, including cancer[11, 15, 16], neurodegenerative disorders[17, 18] and infectious diseases[19, 20]. In this Primer, we provide an overview of the principles, applications and future prospects of HT in biological research. We will discuss the diverse HT techniques, their benefits and limitations as well as the challenges and opportunities in crafting HT-based diagnostic and therapeutic strategies. We will also spotlight recent advancements in HT and its potential impact on various areas of biomedical research.

Experimentation

Coherent HT

Coherent HT capitalizes on spatiotemporally coherent light illumination to render 3D label-free images of live cells. The preference for coherent sources stems from initial design and theory of optical tomography, assuming single-wavelength light propagation[21, 22]. Coherent HT reconstructs the 3D RI distribution of samples by capturing their microscopic images under sequential illumination at multiple illumination angles (Fig. 1c). To reconstruct the RI of the sample, both the phase and intensity of the light transmitted through the sample are needed. Imaging the phase is not straightforward as cameras only measure light intensity. Techniques for retrieving the phase of light from intensity measurements are broadly known as QPI. In essence, coherent HT methodologies incorporate a QPI configuration augmented with an apparatus that scans the angle of the illumination. Most techniques differ either in the illumination scanning apparatus or in the QPI configuration employed for phase retrieval.

QPI and related phase retrieval can be performed in numerous ways. Traditionally, Mach–Zehnder interferometric techniques have been widely used as simplistic approaches to produce a sample and a reference beam from an illumination. A Mach–Zehnder interferometer operates by splitting a laser beam, directing one part through the specimen and the other along a reference path. The two beams are then re-combined using a beam splitter, forming an interference pattern at the camera, enabling retrieval of both the phase and the intensity of the transmitted light field (Fig. 2a). The sample and reference beams can either meet at an angle (known as off-axis holography[23]) or be parallel with a modulated reference beam phase (known as phase shifting holography[24]).

Self-interfering QPI configurations have been developed, offering enhanced stability and more compact instrumentation compared with traditional interferometry. Coherent HT, when implemented with a separate reference beam, can be susceptible to instability stemming from mechanical vibrations, and requires a sizeable area to accommodate dual beam paths. Conversely, self-interfering setups operate without a reference beam, interfering the sample-diffracted beam with itself to retrieve phase information. Broadly used methodologies include: using a known[25, 26] or filtered[27] area of the sample-diffracted beam to form decodable interference patterns; shearing interferometry, which interferes the sample-diffracted beam with the slightly shifted copy of itself to retrieve the derivative of the phase[28]; phase retrieval based on the Kramers–Kronig relations [29] and an algorithm from redundant measurements at different depths or illumination angles[30, 31]. Nevertheless, self-interfering coherent HT has its own challenges, including complications in beam steering, constraints related to sample density and low precision in the reconstruction of low spatial frequencies.

To accomplish illumination angle scanning, active beam-steering hardware is commonly used. This category includes devices such as micro-electromechanical systems[32], galvanometric mirrors[33, 34, 35], spatial light modulators[36] and digital micromirror devices[ ] of incident light. Finally, angular scanning can be achieved by rotating the sample while maintaining a

constant illumination direction[38, 39]. Although these strategies can counteract a potential loss in axial resolution, their application remains limited when dealing with live biological cells or arbitrarily shaped samples.

Temporally low-coherence HT

Recently, incorporation of low-coherence sources appears to resolve the undesired artefacts from coherent HT, such as the speckle noise. Some of the principles and methods developed for coherent HT can employ spatially coherent yet temporally slightly incoherent light. This approach effectively mitigates speckle noise and fringes induced by back reflections in the optical system while still enabling reconstruction under the monochromatic assumption[36, 40]. Alternatively, multiple light sources such as those implemented in light-emitting diode (LED) arrays can be sequentially turned on and off to vary the illumination angle[30]. These low-temporal-coherence conversions provide higher signal-to-noise ratios (SNRs) with small modifications in the fundamental design but entail distinct difficulties as well. From a technical perspective, precisely matching beam paths within the short coherence length may be difficult to achieve. The rapid decorrelation of light along the propagation may complicate the imaging of thick samples unless augmented with mechanical scanning.

Spatially low-coherence HT

Spatially incoherent light can be conceptualized as a superposition of multiple incoherent beams with varying incident angles. Illumination light beams are incoherent in that they do not interfere with each other: the total intensity measured by the camera is the sum of the intensities of the transmitted field for each illumination.

Low-coherence HT is enabled by the weak scattering approximation under which the intensity is linearly related to the RI and absorption[41]. As such, the incoherent sum of transmitted intensities is also linearly related to the RI. A phase retrieval-like problem remains; we need to differentiate between the RI and absorption of the sample. The absorption can be viewed mathematically as the imaginary part of the RI. For this reason, methods analogous to phase retrieval are used to distinguish absorption from refraction using redundant information from multiple illumination[42, 43], transparent sample assumption[41, 44], phase shifting interferometry[45], shearing interferometry[28, 46] or the Kramers–Kronig relations[47].

The low-coherence HT illumination is typically generated using an LED in combination with a mask[41, 44, 45, 48], a microdisplay[43, 49] or an array of LEDs[42] (Fig. 3b). The microdisplay or LED array is positioned at the pupil plane of the microscope condenser so that each pixel corresponds to a particular illumination incidence angle at the sample plane. The chosen intensity at the pupil plane is highly dependent on the low-coherence HT modality. Shearing interferometry-based methods fully illuminate the pupil plane of the condenser. Methods based on redundant information from multiple illuminations usually illuminate only about half of the pupil plane at once. Finally, methods based on phase shifting interferometry illuminate a thin ring in the pupil plane.

Fig. 3

Optical measurement and numerical reconstruction in holotomography.

a, An interferometric instrumentation for coherent (or temporally low-coherence) holotomography (HT). The illumination is split into the illumination and reference beams with a beam splitter. In the illumination path, the illumination angle is scanned with a beam-steering compartment. This example shows projecting different grating patterns on the spatial light modulator to this end. The complex field of the scattered light is captured at a series of illumination angles, retrieved from the interference of the sample-scattered beam and the reference beam. This angular stack of the optical field (the intensity and phase) is mapped onto the scattering potential in Fourier space. The RI is obtained from the assembled scattering potential through Fourier transform. **b**, An axial scanning instrumentation of spatially low-coherence HT. The intensity of the scattered light is recorded while modulating the illumination aperture. This example shows projecting four different aperture intensity profiles using the spatial light modulator to this end. The axial stack of intensity measurements is converted to RI by deconvolving with the optical transfer function, which is predetermined by the aperture modulation. In both approaches, regularization based on previous knowledge of the sample can be applied to enhance the quality of RI reconstruction. The missing cone is depicted with a green shade in each transfer function. LED, light-emitting diode; RI, refractive index.

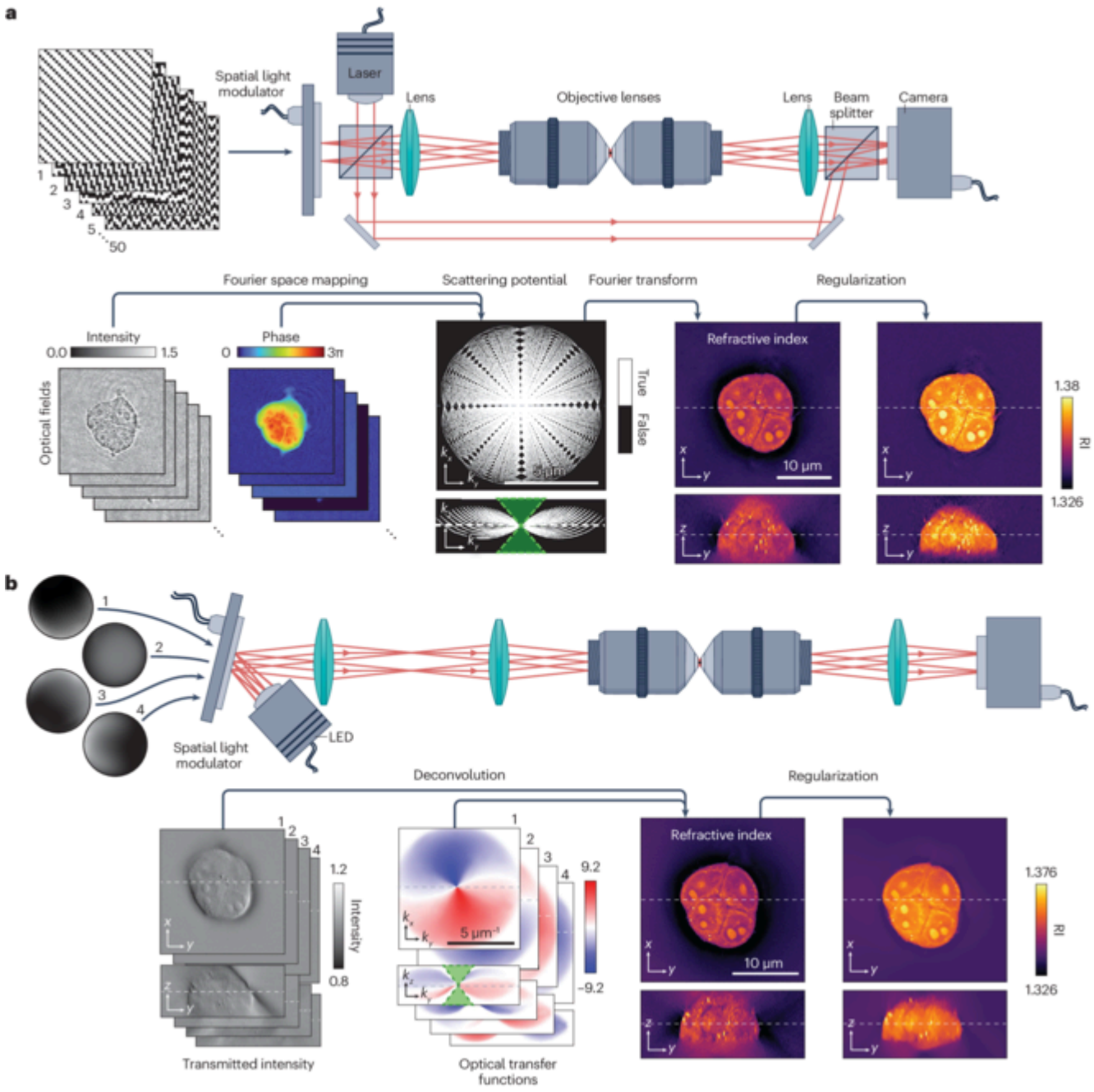

Owing to its use of incoherent light, low-coherence HT possesses inherent sectioning capability. Axial scanning must be performed to obtain volumetric information about the sample, in contrast to coherent HT, in which angular scanning is used. Axial scanning is usually performed by directly moving the sample, but faster scanning can be performed using liquid lenses[44] or remote focusing[43].

Spatially low-coherence HT offers improved sample penetration depth when compared with coherent HT or temporally low-coherence HT[46]. This advantage largely stems from the averaging of many illumination modes, resulting in the dampening of interference patterns caused by multiple light scattering within a sample. Phase unwrapping is also not used in spatially low-coherence HT, reducing discontinuity in the image. Imaging thick (more than a few hundred microns, such as organoids and adult *Caenorhabditis elegans*) or porous biological samples (such as hydrogel-embedded cells) remains a challenge owing to significant AQ6 multiple scattering[50, 51]. Nevertheless, innovative methods are being developed to overcome these limitations, as will be partially introduced in the following section.

Comparing illumination strategies

Understanding the strengths and weaknesses of different HT experimentations is necessary to select the most suitable HT option for a given research environment and target application. Coherent HT and temporally low-coherence HT generally provide high temporal resolution, but the mechanical vulnerability of the bulky setup, along with the limited imaging depth, may pose an issue. Therefore, these HT configurations are generally better suited to studying the dynamics of a small number of cells, particularly when sufficient and stable space for optical experiment is provided. By contrast, spatially low-coherence HT offers high SNR and deep imaging at the cost of the image acquisition rate. Therefore, spatially low-coherence HT offers a solution for investigating tissues and 3D cultures in extracellular matrix.

Reconstruction and regularization

The process of HT reconstruction starts with phase retrieval. Typically, coherent HT uses off-axis or phase shifting interferometry to retrieve the field transmitted through the sample E_{sample} from the intensity measured at the camera .. In interferometry, a reference plane wave . is interfered with the transmitted field E_{sample}. If . denotes the reference field wavevector, . the spatial coordinate and . the global phase:

1

The sample field can be obtained AQ7 from term #2 but contributions from terms #1 and #3 need to be deduced. Phase shifting interferometry measures I_{Camera} with three or more . values to separate each term contribution[52]. Alternatively, off-axis holography increases the lateral component of the wavevector . so that each of the three terms is located at a different position in the Fourier plane, enabling retrieval of E_{sample} from a single camera image using Fourier space filtering[23].

Then volumetric HT reconstruction bears considerable similarity to other tomographic techniques such as X-ray CT (Fig. 3). In an interferometric coherent HT (Fig. 3a), illumination of the sample from a specific direction results in an image, which can be considered a projection of the sample along that same direction. As projections correspond to sections in Fourier space, the acquired data undergo a

Fourier transformation and are positioned appropriately in the Fourier plane of the sample via filtered back projection. The key distinction between HT and CT lies in the fact that the wavelength of the visible light is much larger than the X-rays used in CT, rendering diffraction a significant consideration[22, 53]. To account for this factor, the section plane onto which the data are projected in the Fourier space is curved. This leads to an enhanced version of filtered back projection, referred to as the Fourier diffraction theorem [53].

Two versions of the Fourier diffraction theorem are used: the Born approximation and the Rytov approximation. The Rytov approximation linearly relates the RI to the phase of the transmitted field and is generally more accurate[54, 55]. By contrast, the Born approximation linearly relates the field to the RI enabling easier computations, especially in the presence of incoherent light[41]. According to the Born approximation, the field scattered by a scattering potential ., a function of the RI . given by . with . the mounting medium RI, is:

2

in which the Green's function[53, 56] . denotes the light field detected at the camera in the case in which the sample is a point source and . is the convolution operator. Here . is the axial component of the wavevector with . the wavenumber in the mounting medium. The Fourier transform of the Green's function corresponds to a spherical cap so that this equation can be interpreted as the field information corresponding to the sample information positioned on a sphere cap in the Fourier plane. As such, the field information is projected on various spherical caps corresponding to each illumination angle, slowly filling the Fourier plane of the reconstructed sample.

The Fourier diffraction theorem forms the basis of all HT techniques employing linear reconstruction. Variants of the Fourier diffraction theorem have also been derived for anisotropic materials enabling imaging of birefringence strength and direction[57, 58, 59]. Even HT using spatiotemporally incoherent light computes the optical system response by adding the different back-projection planes that correspond to the angular decomposition of the incoherent illumination[41, 60]. The image formation is then described by a convolution of the RI with a point spread function PSF. More precisely, the absorption and RI are convolved with a different point spread function. The PSF for the real part of the scattering potential (corresponding to the RI) is often called the phase point spread function PSF_P, whereas the PSF for the imaginary part of the scattering potential (corresponding to the absorption) is often called the absorption point spread function PSF_A. Those PSF can be formulated as the product of a Green's function corresponding to the detection (equation (4)) with one corresponding to the illumination[41, 61] (equation (5)):

3

4

5

With . corresponding to the intensity distribution at the pupil plane[61], . denotes the Fourier transform and * is the convolution operator. This formulation is similar for most incoherent HT configurations with slight alterations depending on the optical system. For example, configurations based on phase shifting do not require the real and complex parts in the PSF[45], and shearing interferometry PSF requires further modifications to the Green's functions[62]. The RI can finally be obtained using a deconvolution algorithm[41]. Deconvolution practically means Fourier transforming the experimentally measured 3D intensity stack, dividing by the Fourier transform of the PSF while using a regularization and finally doing an inverse Fourier transform to obtain the RI[41, 43] (Fig. 3b).

The linear algorithm falls short when applied to highly scattering objects. In such instances, nonlinear reconstructions based on accurately simulated light propagation become necessary[50, 63, 64, 65, 66, 67, 68]. The reconstructed RI tomogram can be iteratively enhanced by comparing the simulated and experimental light fields and by back-propagating the error utilizing a time-reversal light scattering simulation.

Missing cone problem

One limitation of HT is the missing cone problem, wherein not all information about the Fourier plane of the object can be retrieved owing to the maximum illumination angle being constrained by the optical system (as depicted by the shaded region of transfer functions in Fig. 3). This issue can generate artefacts such as vertical sample elongation or low RI regions known as the halo effect. To address this problem, regularization algorithms have been devised to fill in this missing information using previous knowledge about the sample[69] (Table 1).

Table 1

Categories of regularization algorithms for reducing missing cone artefacts

Algorithm	Principle	Strengths	Weaknesses	Examples
Gerchberg–Papoulis	Enforcement of previous constraints while alternating between spatial and frequency domains	Missing cone mitigation while preserving measured signal	Noise amplification	Gerchberg (1974)[70] Lim et al. (2015)[69]
Edge preserving	Smoothing of image selectively outside the detected edge	Preservation of sharp features	Moderate missing cone mitigation and considerable computational load	Charbonnier et al. (1997)[78] Lim et al. (2015)[69]
Total variation	Reduction of derivative gradient while maintaining image fidelity	Robustness in a wide range of images	Staircase artefacts, parameter dependence and large computational load	Lustig et al. (2007)[72] Rudin et al. (1992)[73] Lim et al. (2015)[69]

Algorithm	Principle	Strengths	Weaknesses	Examples
Hessian	Reduction of second-order image derivative while maintaining image fidelity	Reduced smoothing artefacts	Parameter dependence and large computational load	Lefkimmiatis et al. (2013)[74] Pham et al. (2020)[75]
Artificial intelligence regularizer	Statistically optimized prediction of the improved image from a given image	Fast inference	Requirement of training and potential generalization issues	Zhou and Horstmeyer (2020)[82] Yang et al. (2020)[84] Chung et al. (2021)[81] Lim et al. (2019)[63] Ryu et al. (2019)[83]

The most prevalent previous information used is non-negativity, or the Gerchberg–Papoulis algorithm, as most samples possess an RI higher than their mounting medium[70]. Another commonly employed previous constraint is total variation[71, 72, 73], which capitalizes on the fact that most samples have sharply defined edges connecting piecewise constant RI regions. More advanced regularizations such as Hessian Schatten norm[63, 74, 75] or edge-preserving regularization[76, 77, 78] are predicated on similar principles, and regularization using the object support[79] or for polarization-sensitive measurements[80] has also been developed. Finally, regularization based on artificial intelligence is also demonstrating promising results[81, 82, 83, 84].

It is crucial to acknowledge that the missing cone problem is not exclusive to HT but is also prevalent in other imaging fields[85, 86] including wide-field fluorescent imaging[87], limited-angle CT[88], MRI or transmission electron microscopy[89]. A range of regularization algorithms have been developed for these techniques that could be adapted for HT[69, 80, 90], whereas several latest algorithms have yet to be applied in HT[91, 92, 93, 94]. The choice of the regularization method, at a given sample and imaging condition, would be decisive to the extent of image improvement. Yet, it has been investigated in only a small scale and limited set of samples and algorithms thus far[69]; the findings included the weakness of Gerchberg and Papoulis under noise, effective mitigation of image elongation by total variation and the efficiency of edge preserving when given high numerical aperture. By contrast, recent efforts using artificial intelligence to construct regularization pipelines[81, 82, 83, 84] have shown promise in the speed and adaptivity.

Sample preparation

Owing to its label-free characteristic, HT mandates only minimal sample preparation, with labelling or fixation remaining an optional step for correlative studies of HT and label-specific imaging. The sample preparation in HT typically includes placing the sample on a compatible slide or within a suitable container without the need for labelling or fixation agents. This can involve simple procedures such as cell culturing in appropriate media, ensuring that the sample is live and in a natural state for imaging. However, certain mechanical conditions must commonly be considered for HT acquisition, such as maintaining slide thickness below the working distance, particularly when using objective lenses with high numerical aperture. High numerical aperture objectives are largely adopted in HT realizations for high resolution (with the exception of ptychographic methods[95, 96]), yet they feature notably short working distances. To accommodate deeper imaging, using a sample container with a thin bottom substrate, such as a 1.5H glass slide, is recommended. Alternatively, using high numerical aperture objective lenses with long working distances can effectively extend the imaging depth. When using well plates, a particular condition is that the walls of the wells should not interfere with the light path for high-angle illumination, to achieve the desired illumination profile at the sample location. An advisable precaution would be selecting well plates with low-profile walls or using specialized imaging wells designed to minimize optical interference.

Additionally, it is essential to minimize sample motion during each series of measurements for HT, which may result in artefacts. Although this condition applies to any HT experimentation, particular attention is called for in case of HT realizations involving large number of measurements such as ptychographic or scattering-based methods. Naturally steady samples — such as adherent mammalian cells — can be imaged without heavy constraints. However, certain suspension samples, such as bacteria, yeast and non-adherent cells, may require immobilization to guarantee robust HT reconstruction. Coating the imaging substrate with concanavalin A or implementing a 3-aminopropyltriethoxysilane modification facilitates cell binding non-specifically to the surface[97]. Alternatively, the topography of the sample holder itself can be used to immobilize or trap samples. For instance, the elastic and transparent material polydimethylsiloxane can efficiently immobilize and trap cells between polydimethylsiloxane and the base cell culture glass. This approach has been successfully used to image pre-aligned cells (such as budding yeast) in a single focal plane for time-lapse imaging[98, 99]. Recently, a hydrogel was used to immobilize individual live bacteria for the HT measurements[100].

Results

Label-free volumetric imaging of cells

HT has been extensively employed for 3D imaging of living cells, offering a solution to the limitations of label-dependent methods that necessitate labelling, fixation or sectioning[101, 102, 103, 104]. HT does not require the fixation of cells, thereby permitting the measurement of live cells in their natural state (Fig. 4a). This also confers practical benefits such as simplicity of measurement and minimal phototoxicity. The 3D RI image of a cell delineates the entire cell morphology, including lamellipodia and dendritic shafts, as the RI of the cytosol exceeds that of the surroundings. Moreover, intracellular RI variation facilitates spatial distinction between major

Fig. 4

Label-free 3D imaging of diverse live cells.

A, Two-dimensional RI distribution images of various cell types: neuro-2a cell (part **Aa**) and mouse primary neuron (part **Ab**). Neuro-2a cells depict a triangular structure with short, blunt neurites. Mouse primary neurons present extensive neurites and a large nucleus consuming most of the cytoplasm. The colour bar indicates the 2D RI range. Parts **Ac** and **Ad** show 3D models reconstructed using 3D RI distributions corresponding to parts **Aa** and **Ab**, respectively. The adjacent colour bar denotes the 3D RI range. **B**, Two-dimensional RI distribution image of adipocytes differentiated from fibrocytes, with zoom-in images of adipocytes in the inset. **C**, Time-lapse image of Hep3B cells illustrating subcellular morphology changes upon H_2O_2 treatment, followed by cellular recovery after returning to the regular cell culture medium. HT, holotomography; RI, refractive index.

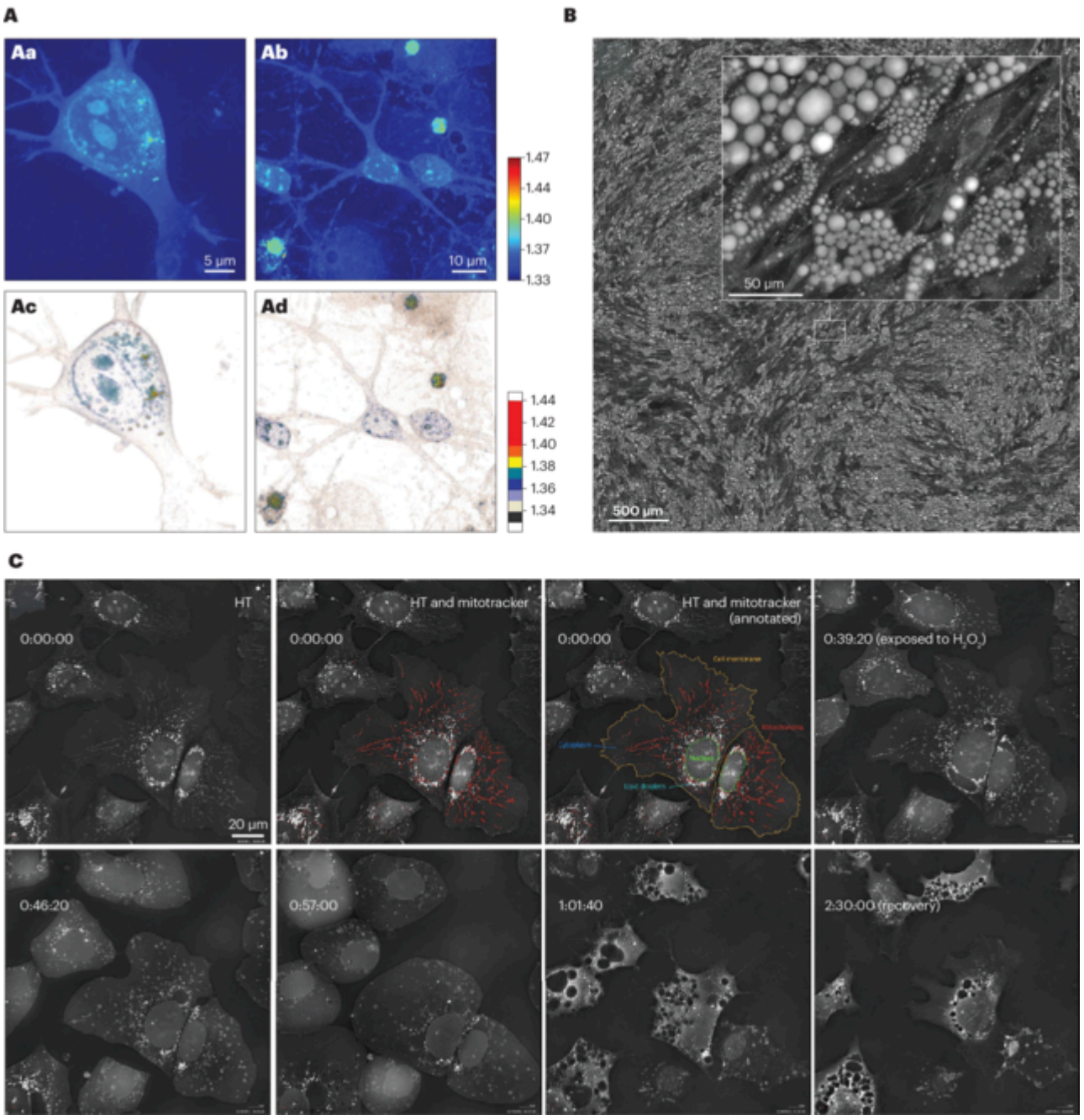

The label-free imaging of unlabelled cells using HT facilitates the long-term assessment of individual cells in their native states. This ability can further generate synergistic effects when combined with the quantitative phase capability. The RIs of lipids droplets are distinctly higher than those of cytoplasm and other subcellular organelles[105], and the lipid droplets are readily localized in the 3D RI tomograms of unlabelled cells. The volume and mass of each lipid droplet can be quantified, whereas the lipid species composition and their mole fractions determine the RI value[106, 107].

The field of view of HT is generally determined by the specifications of the objective lens, image sensor and the overall magnification of the optical configuration. For high-resolution imaging, the objective lenses with high numerical aperture are usually adapted and thus the field of view is limited to 100–200 µm. However, the lateral size of HT images can be expanded by measuring multiple fields of view and stitching them after reconstructions[8]. Figure 4b shows an example of the large field-of-view image of HT — the 4 mm × 4 mm stitched RI tomogram of fully differentiated adipocytes from the induced stem cells.

Different subcellular organelles exhibit different RI values, and thus the precise HT measurements visualized major subcellular organelles without fluorescence labelling (Fig. 4c). The cell membrane and nucleus membrane can be distinctly visualized owing to the contrast of RI among the surrounding medium, the cytoplasm and the nucleoplasm. Lipid droplets have distinctly high RI values in cytoplasm and can be easily localized and quantified[108]. The nucleolus has RI values higher than the surrounding nucleoplasm. Mitochondria also have higher RI values compared with the cytoplasm. These RI characteristics of major subcellular organelles enable versatile quantitative intracellular analyses.

Quantitative analysis

The numerical processing of data stands as a fundamental component of HT. Each HT variant involves a numerical process that translates a series of 2D measurements into the 3D RI distribution. In most HT implementations — particularly coherent HT — the angular sinogram of 2D optical fields is mapped onto the spatial frequency domain scattering potential[35]. In another category, a focal stack of

verted into the 3D RI image via deconvolution with the optical transfer function[42, 43, 61, 109].

Regularization is frequently applied to enhance reconstruction quality. This is particularly useful for addressing the issue of low axial resolution that results from the limited-angle configuration of the imaging hardware[69, 83]. The resolution limit can be mitigated by enforcing constraints that reflect previous knowledge about the sample.

After reconstruction, the size and biophysical parameters of subcellular organelles and whole cells can be derived directly from each HT image[110]. From the reconstructed RI tomograms of cells, key subcellular organelles such as the cell membrane, nucleus membrane, nucleoli, lipid droplets and mitochondria become easily identifiable, owing to the RI contrasts between these organelles and the surrounding cytoplasm or nucleoplasm. Both manual and automatic segmentation algorithms, whether rule-based or powered by machine learning, facilitate the measurement of the size and volumes of these organelles. This enables subcellular analyses without the need for cell fixation or staining, maintaining the cells in their natural state. Although subcellular analyses of HT still rely largely on manual segmentation, advanced platforms that use machine learning to accelerate this procedure have been developed in other fields[111, 112, 113]. These tools will effectively reduce the amount of labour and time needed, but the applicability may need adjustments as their primary target domain is different from HT.

The unique quantitative nature of RI allows for the quantification of biomolecular contents and concentration of cells and their subcellular organelles. Specifically, RI indicates the composition at each volumetric location; for the aqueous solution that constitutes living cells, RI linearly increases with the concentration of molecules such as protein[114]. As a HT image depicts the 3D arrangement of biomolecules, a biological sample can be distinguished from its environment in 3D. The sample volume can be ascertained by tallying the number of voxels within the defined envelope. The envelope also allows for the acquisition of other morphological properties such as surface area and sphericity. Moreover, integrating the RI contrast over these voxels yields the gross amount of biomolecules contained within the sample, that is, dry mass[114, 115]. The RI distribution also provides details such as the average and variation of dry mass density.

The analytical advantage of RI has supported distinct studies and applications that quantitatively examine live cells. For instance, an active field of study involves identifying alterations in the properties of individual red blood cells (RBCs) under various pathophysiological conditions[35, 110, 116, 117, 118]. Other applications include continuous monitoring of bacteria[19, 100, 119], tracking lipid droplets in hepatocytes[105] and characterizing neuronal growth[17].

Quantifying subcellular structures

HT allows for the quantitative characterization of the morphological and biophysical properties of subcellular organelles with a spatial resolution approaching 100 nm (ref. [120]). Leveraging the quantitative information procured through HT, which illustrates the physical characteristics of subcellular organelles, aids in constructing comprehensive models for a deeper understanding of biological processes.

The cell nucleus has a critical role in preserving cell physiology through genetic transcription and gene expression. Traditionally, the nucleus has been viewed as one of the densest organelles in cells as all genetic materials, in the form of a linear DNA polymer ~2 m in length, are packed into a small sphere roughly 10 μm in diameter. However, QPI and HT have demonstrated that the cell nucleoplasm possesses a lower RI than the surrounding cytoplasm in suspended cells[121] and cells grown on a 2D substrate[33, 122], signifying a lower mass density in the nucleoplasm. A recent study showed that the relative mass density difference between the nucleoplasm and the cytoplasm is consistently preserved during cell cycle progression, as well as during drug-induced alterations of cytoskeletal polymerization and chromatin condensation[122]. The inversion of this usually robust relative mass difference has so far been observed only in unique conditions such as cells cultured in a 3D hydrogel[123], cells under hyperosmotic shock[124], blood cells[125] and light-guiding photoreceptor cells in the retina of nocturnal mammals[121]. Additional studies are necessary to decipher the mechanism through which the mass density difference across the nuclear envelope is maintained, as well as any potential biological implications of this phenomenon.

HT has also elucidated other subcellular organelles, particularly those formed through phase separation and transition[126]. A key example is nucleoli within nuclei, which are instrumental for the synthesis and assembly of ribosomal subunits used in protein translation. Recent research has revealed that nucleoli are membrane-less compartments formed by liquid-liquid phase separation and possess unique biochemical and viscoelastic properties[127]. In the RI tomograms reconstructed by HT, nucleoli consistently show a higher RI than the surrounding nucleoplasm. Their physicochemical attributes have been examined in various conditions such as cell cycle progression, drug treatment or ATP depletion[122, 128, 129].

Mitotic chromosomes, which are condensed forms of chromatin during cell division, display distinctively high RI values when analysed using HT[77, 130]. The elevated RI values of chromosomes under hyperosmotic conditions were linked with molecular crowding[130]. Furthermore, dual-wavelength HT using visible and ultraviolet wavelength beams unveiled the dispersive properties of chromosomes and cytoplasm[77]. Conversely, HT measurements on mitotic spindles in the *Xenopus* egg extract demonstrated that the spindle, typically described as a condensed phase of microtubules and associated proteins in the cytoplasm, actually possesses the same density as the surrounding cytoplasm[131].

The mechanical and dynamic properties of organelles have also been investigated using HT with high temporal resolution; coherent HT with illumination scanning has achieved 3D imaging at a rate of 100 Hz (ref. [37]). A study that tracked lipid droplets in 3D through HT revealed the heterogeneity of intracellular lipid dynamics and the negative relation between the diffusion coefficient and the exponent[105]. Another study used HT to evaluate the rotation of nucleus and lipid droplets, in which the revealed synchrony of the rotation implied that the entire nucleus spins[132]. Mitochondrial dynamics have been investigated with time-lapse HT, which enabled quantification of the interaction time between the mitochondria and other organelles[132, 133].

Although HT provides 3D quantitative imaging of unlabelled cells in 3D, its lack of molecular specificity can be a limitation. To offset this, HT has been integrated with fluorescence microscopy techniques such as epi-fluorescence[121, 134], confocal fluorescence[77, 135] and structured illumination microscopy[133, 136, 137]. Through the correlation of fluorescence emission signals with reconstructed RI tomograms, it is possible to perform synergistic analyses that provide both structural and molecular insights about cells, similar to the way in which PET/CT is used in medical imaging. This allows the determination of local mass density for subcellular organelles and specific proteins, from which measurable data such as dry mass, volume and mass density can be extracted. Additionally, juxtaposing confocal fluorescence volumes with reconstructed RI tomograms provides extra 3D morphological constraints, enhancing the precision of tomogram reconstruction using the Gerchberg–Papoulis iterative algorithm and minimizing missing cone artefact[138].

Implementing vibrational spectroscopy in conjunction with HT enhances molecular specificity in a label-free manner. This collaborative technique facilitates the identification of the chemical composition within subcellular compartments. It has been used in phenotyping the metastatic propensity of cancer cells[139] and in determining the saturation degree of lipid droplets in preadipocytes[140]. Recent advancements in Raman spectroscopy enable quantitative assessment of the density of substances such as protein, lipid and water[141], as well as the prediction of the RI values of samples based on Raman scattering intensity at diverse vibrational modes[142]. HT can supplement this information on mass density and RI, providing a benchmark for these recent achievements, and the precise chemical compositions ascertained through these methods can be used to estimate the corresponding RI increment. In combining HT with vibrational spectroscopy effectively, these techniques can be implemented either sequentially or simultaneously, depending on the specific experimental setup and objectives. Sequential implementation involves first acquiring HT images to visualize and measure the 3D RI distribution of cells or tissues, followed by vibrational spectroscopic imaging to analyse the chemical composition of the same sample areas. This approach allows researchers to correlate physical properties, such as cell volume and mass density obtained from HT, with chemical information, such as lipid and protein concentrations, from vibrational spectroscopy.

Additionally, Brillouin microscopy has surfaced as a spectroscopic technique to quantitatively depict the mechanical properties within biological samples[143]. This technique involves the measurement of the inelastic Brillouin frequency shift, caused by the interaction between photons and internal acoustic phonons of the material. Consequently, Brillouin microscopy allows an all-optical characterization of the longitudinal modulus (inversely proportional to linear compressibility) and viscosity of biological tissues and cells at a resolution limited only by diffraction[143, 144]. Integrating Brillouin microscopy with HT can enhance the accuracy of longitudinal modulus calculations based on the measured Brillouin frequency shift, considering the local RI and density data provided by the HT. This integrated methodology has proven useful in studying the mechanical and physical attributes of microgel beads[145], protein condensates[146], cells[123, 146], lipid droplets in adipocytes[146, 147] and in the context of tissue regeneration[144, 148].

Extracting physical properties from individual organelles leads to quantitative biophysical insights; for instance, the flow of biomolecular mass can be traced throughout important phenomena such as mitochondrial fission, fusion[149] and lipid–mitochondria interaction. Experimental precision is necessary to effectively achieve such subcellular investigations. For instance, measuring both imaging modalities within the timescale of sample dynamics is advisable to register the images without technical difficulties. Furthermore, different modalities are likely to provide unidentical resolutions, necessitating accurate resampling of the correlative measurements.

Applications

The applications of HT in various scientific fields underscore its transformative impact on basic and preclinical research. In haematology, HT identifies blood cell pathologies and characterizes immune cells, enhancing our understanding of diseases such as malaria and diabetes. Microbiology benefits from the real-time analysis of HT of bacteria and yeast, bypassing the limitations of traditional labelling methods. Studies on lipid metabolism leverage HT to monitor lipid droplet dynamics, crucial for metabolic disease research. HT also supports the investigation of phase-separated biomolecular condensates, contributing to our understanding of cellular physiology. In stem cell research and embryogenesis, non-invasive imaging of HT facilitates the study of stem cell biology, developmental biology and regenerative medicine. The application of technology extends to 3D cell culture, organoids and histology, in which it provides detailed, quantitative data on tissue architecture and function, promising advancements in disease diagnosis and therapeutic development.

Microbiology

Microbiology stands to gain considerably from rapid, label-free measurements of HT. Although fluorescence imaging[150] and electron microscopy[151] are frequently employed in image-based bacteria studies, their inherent need for labelling and associated detrimental effects hinder real-time investigations of live bacteria (Fig. 5). By contrast, HT offers non-invasive, continuous morphological analysis of undisturbed microbes. Yeast is an excellent model for studying the cell cycle, metabolism and signalling owing to its easily modifiable genetics and shared biological components with human cells. Recent studies have highlighted a notable shift in the intracellular environment of yeast under glucose deprivation, which is marked by a reduction in macromolecule movement in glucose-deprived yeast, as observed through fluorescence-based measurements[152]. HT proves a highly effective platform for exploring cell dynamics over extended periods or with high temporal resolution[125], providing biophysical information — such as biomolecular concentration, dry mass and properties of subcellular structures — without the need for labelling, facilitating studies on yeast responses to glucose deprivation and osmotic stress[153, 154].

Fig. 5

Applications of holotomography in microbiology.

a, Yeast cells captured by a holographic optical tweezer[39]. The central axial slice (upper) shows heterogeneity of refractive index (RI) [Loading web-font TeX/Caligraphic/Regular]ch subcellular structures can be identified as marked in the volumetric rendering (lower). **b**, Time-lapse

monitoring of growing bacteria[19]. The central axial slices (upper) and the corresponding volumetric renderings (lower) are shown after 0, 120 and 240 min of culture. Part **a** reprinted with permission from ref. [39], Optica. Part **b** reprinted with permission from ref. [19], Optica.

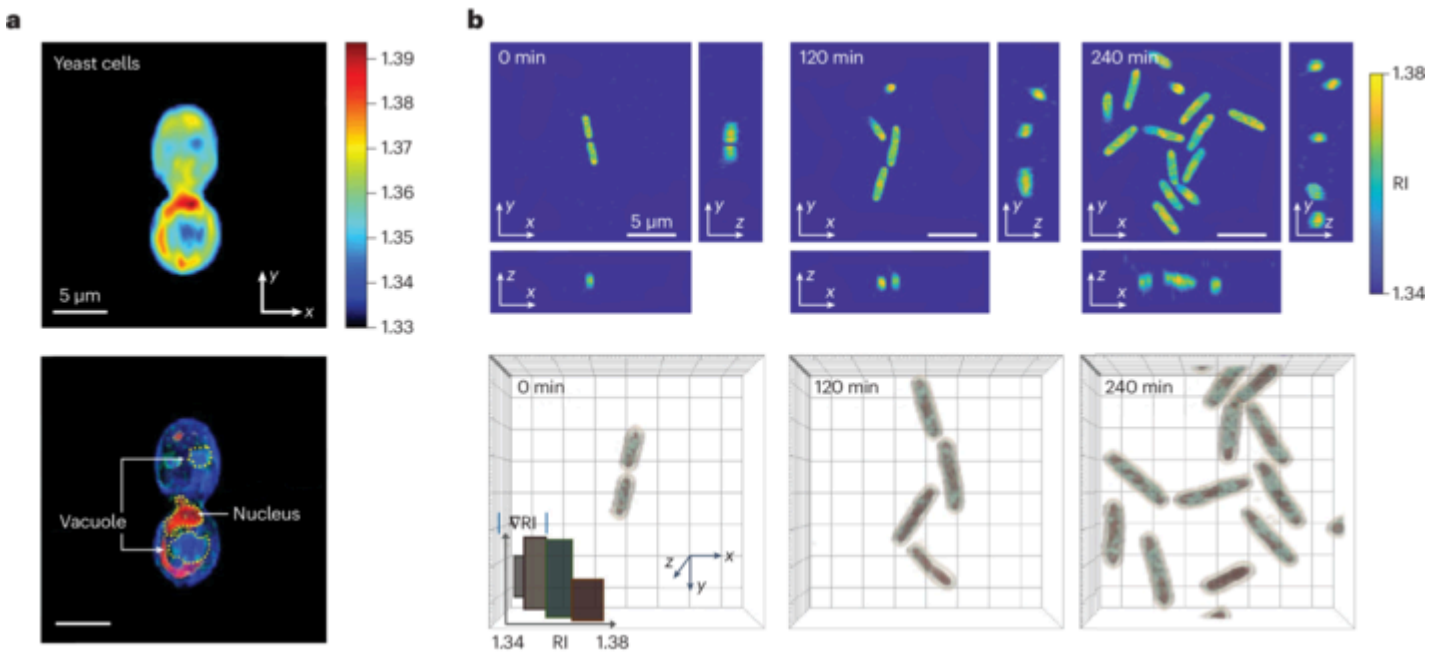

HT has demonstrated time-lapse imaging of bacteria growth in the presence of antibiotics[19], accelerating pathogenic profiling in clinical microbiology (Fig. 5b). The analysis of HT images aided by artificial intelligence has achieved species-level identification from individual bacterial clusters, potentially reducing the time required for standard microbial identification using in vitro cultures[20, 155]. In antibiotic susceptibility testing, HT enables single-cell characterization of bacterial responses to antibiotics within 2 h (ref. [19]).

In the field of biopolymer biosynthesis using microorganisms, particularly polyhydroxyalkanoates[156], HT offers real-time monitoring of polyhydroxyalkanoate accumulation in live bacteria at the single-cell level[119]. This capability could contribute to the development of sustainable materials, addressing challenges associated with traditional methods relying on bacteria in non-native states[157] or using costly and complex procedures[158].

Haematology

The advancement of QPI and HT has been largely influenced and adopted by applications related to blood cells since their early development. This partially owes to the simple and explicable structure of RBCs, as well as their wide availability. A wealth of research employing HT has illuminated cellular and subcellular modifications in RBCs under various physiological conditions and has compared immune cells in differing environments. Research has shown that HT-based analysis can identify haematological diseases such as malaria[35], sickle cell disease, diabetes, iron-deficiency anaemia, spherocytosis and cardiac arrest[110, 118, 159, 160]. Moreover, HT has provided the means to characterize immune cells, indicating their subtypes and pathophysiology[125, 161]. Recently, the enhanced measurement accuracy of HT has furthered the study of platelets, allowing the identification and quantification of differences in individual platelets in their natural state[162, 163]. Structural and constitutional changes in individual platelets have been observed in two pathological states (a myeloproliferative mutation and following *Leishmania donovani* infection), showing changes in dry mass and the number of high RI structures.

Lipid droplet dynamics

HT is widely used for tracking various subcellular structures, with a focus on lipid droplets owing to their distinct RI distribution compared with the aqueous surrounding within the cell[164]. Lipid droplets play roles in energy storage, lipid metabolism and cell signalling[165]. HT facilitates the analysis of complex lipid droplet dynamics, overcoming challenges faced by traditional imaging methods.

Fluorescence imaging has considerable limitations when used to investigate lipid droplets dynamics. Traditional labelling — using Nile Red, BODIPY or LipidTOX — can disrupt natural processes such as membrane integrity and metabolism[166]. By contrast, clickable lipids offer a bioorthogonal tracking of specific lipid species[167]. Nevertheless, photobleaching, phototoxicity and low temporal resolution remain a substantial hurdle in studying lipid dynamics with most fluorescence-based techniques. HT addresses these issues with a label-free approach that uses differences in RI, enabling non-invasive visualization of lipid droplets. HT offers continuous, high-resolution monitoring of lipid droplet dynamics, preserving their natural state[105], providing critical insights into droplet size, movement and cellular interactions, essential for understanding lipid metabolism and energy storage mechanisms.

Diseases and physiological conditions affecting cellular metabolism can be detected through changes in lipid droplets, which further highlight the capability of HT to profile the lipid content in unperturbed cells. HT has been used to track lipid droplet accumulation in various cell types under different conditions, such as stem cells treated with oleic acid or a cholesterol transport inhibitor[168]. Additionally, monitoring primary bovine umbilical vein endothelial cells with HT under the infection of *Besnoitia besnoiti* displayed changes in the lipid distribution[169]. Changes of lipid in immune cells, captured by HT, were also related to pathology, medicine and molecular biology. HT captured the differences in morphology and lipid content between normal macrophages and foam cells, while quantifying the lipid reduction by treating nanodrug[170]. In a different study, HT identified accumulation of lipid in live T cells with an impaired non-catalytic region in tyrosine kinase, revealing its involvement in lipid metabolism[171].

Cell biology

Phase-separated biomolecular condensates

Although many HT-based studies on subcellular structures have focused on lipid droplets, the cell interior is also populated by numerous biomolecular condensates [126, 127]. Recent research has demonstrated that phase separation processes drive the formation of condensates with distinct compositions from the surrounding protoplasm[172, 173], which are thought to facilitate or inhibit biochemical reactions and provide diverse solvent environments[174]. Abnormal condensation forms have been found in various cancers and neurodegenerative diseases[175, 176]. HT has been used to study the phase behaviours of purified biomolecules and the properties of biomolecular condensates in living cells[177].

In vitro reconstitutions using purified components have been a powerful approach to probe the intrinsic capacity of proteins for phase separation, with HT proving suitable for surveying biomolecular concentration owing to the linear relationship between RI and concentration[114, 178]. Recent studies with purified protein solutions have demonstrated that RI provides higher precision for assessing biomolecular concentration compared with fluorescence intensity-based methods, which tend to underestimate the dense phase concentration[179, 180]. HT is advantageous for examining the phase behaviour of multicomponent systems, directly assessing the total biomolecular concentration in RNA–protein co-condensates[181].

HT can also facilitate the investigation of biomolecular condensates within living cells, providing 3D RI distributions and density information[146]. Nuclear speckles and stress granules are shown to be low-density condensates with their total biomolecular densities similar to the surrounding cellular space[177]. RNA depletion leads to an increase in the RI of nuclear speckles, revealing that RNA has a key role in regulating the density of biomolecular condensates. HT is particularly beneficial for studying intracellular multicomponent condensates, offering unique density information that is inaccessible from labelling specific biomolecules. Yet, as the lack of molecular specificity is also a hurdle in compositional studies, HT can be used in conjunction with fluorescence labelling for outlining and deciphering biomolecular condensates.

Stem cell research and embryogenesis

HT offers a compelling application in non-invasive monitoring of stem cells, particularly human pluripotent stem cells (PSCs) such as induced PSCs (iPSCs). PSCs hold tremendous potential for regenerative medicine, disease modelling and drug discovery[182, 183], and assessing their quality before downstream applications is crucial. Previous studies using phase-contrast and differential inference contrast microscopy established morphological standards for high-quality iPSCs, focusing on colonial border features, cellular characteristics, granular spots and mitochondrial content[147, 184, 185]. However, these criteria lack quantitative contrast and fail to reflect the morphological nuances attributable to the wide variety of subcellular organelles.

Identifying changes in subcellular structures during iPSC transition from their pluripotent state to abnormal cells without labelling has proven challenging to date. Label-free and 3D high-resolution capabilities of HT can address these challenges, providing systematic assessments of unlabelled live iPSCs. For instance, a HT-based study has identified differences between stem cells and fibroblasts; stem cells displayed higher RI in nucleoli and vesicles, whereas iPSCs had fewer vesicles and a larger volume portion of nucleoli[129]. In a colony scale, HT further provides a high contrast in visualizing morphological iPSC evaluation criteria[186] including the boundary definition, intercellular spaces and nuclear morphology (Supplementary Fig. 1a,b), enabling insights into pluripotency and viability and facilitating therapeutic applications of the evaluated iPSCs.

HT shows potential for the study of sperm, oocytes and embryos for in vitro fertilization (IVF), offering quantitative assessments of 3D morphokinetics of bovine and human sperm[187, 188], as well as the 3D visualization of *C. elegans* and bovine embryos[46, 189] (Supplementary Fig. 1c).

Three-dimensional cell culture and organoids

In recent years, cell culture methodologies have shifted from traditional 2D to 3D systems. The increasing inclination towards 3D culture systems arises from its closer mimicry to in vivo conditions, improving drug testing capabilities, accurate tumour modelling and advanced co-culture systems. HT, as a label-free 3D imaging system, is a valuable tool in the studying natural cell behaviour and interactions. High-resolution 3D reconstructions of HT capture intricate spatial relationships, and its non-invasive nature allows prolonged monitoring of samples for insights into short-term and long-term cellular dynamics. The quantitative data aid in precise assessments of cell behaviours and interactions within a 3D environment. HT has been demonstrated for the study of 3D vascularization and tumour spheroids[12, 51].

Organoids are crucial for disease simulation drug discovery and screening[190]. Traditional imaging struggles with organoid morphology, and exogenous labels can hinder cell viability, complicating long-term toxicological studies. Additionally, the size of organoids often surpasses the depth of focus of standard systems such as confocal microscopy, necessitating extensive preparation for imaging. Although light sheet microscopy has improved depth in organoid imaging, it still depends on labelling. To address these challenges, recent research has turned to HT, demonstrating its potential in live organoid assays, by using QPI for thick 3D cell cultures[6, 8, 12, 51, 191, 192] (Fig. 6). These findings suggest that a scalable study on live organoids using HT is near. The application of HT in organoid research is particularly promising for drug screening and toxicity testing[7, 193]; HT has been used to locate and visualize cellular and tissue structures within organoids while maintaining viability. Combining HT with fluorescent labelling strategies, including CRISPR-mediated genetic labelling[194], enhances its capabilities for comprehensive organoid imaging.

Applications of holotomography in the study of organoids.

a AQ8, Time-lapse 3D images of a liver organoid captured using spatial low-coherence holotomography (HT). At the initial time point (left and middle), one can locate a non-dividing cell (circled and magnified) with visible features (red: cell outline, yellow: nucleus, purple: nucleoli). After 20 min of culture (right), a neighbouring cell (magnified) is observed undergoing mitosis, indicated with the chromosomal condensation and alignment. **b**, Correlative imaging exploiting HT and 3D fluorescence microscopy. Correlative imaging potentially provides individual cell analysis, as labelling actin (red) outlines cell boundaries and labelling nuclei (blue) distinguishes each nucleus from the cytoplasm of the cell.

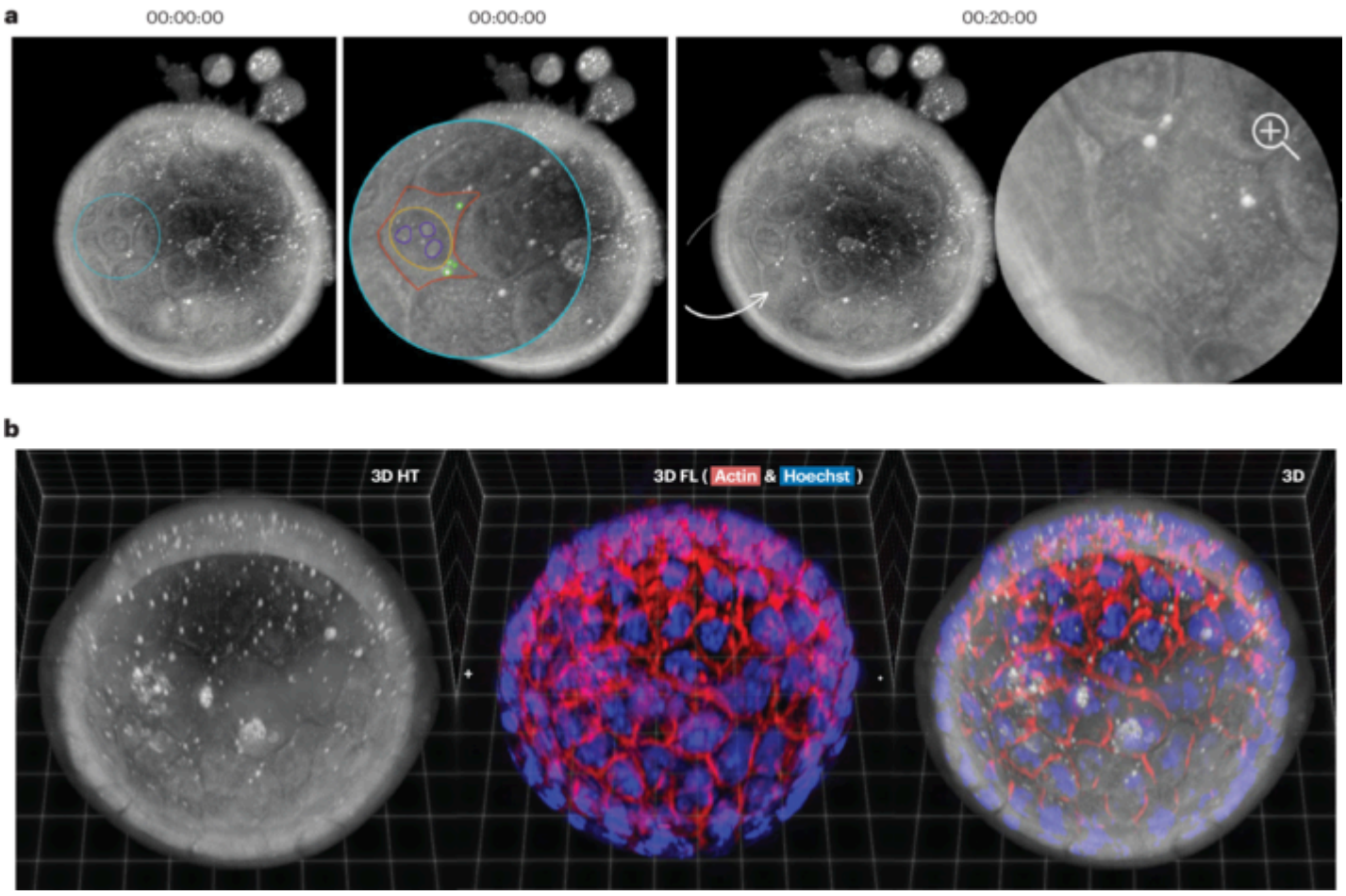

Theragnosis

HT is identified as a potential theragnostic tool for various diseases. Time-lapse HT shows promise in atherosclerosis theragnosis, by demonstrating suppressing lipid droplet accumulation in foam cells with nanodrugs[170]. Similarly, an in vitro model for respiratory pathology can be demonstrated with HT, such as monitoring the apoptotic reaction of lung cells when microplastic particles are introduced[195]. Parasitic activities in live cells can also be identified through HT, as well as the drug-induced egress of the invading parasites[196]. Cancer is another feasible target for HT-assisted theragnosis. HT was able to characterize the therapeutic effects of superparamagnetic iron oxide nanoparticles[197] and bioluminescence-induced proteinaceous photodynamic therapy on cancer cell lines[198]. In addition, HT can aid in future gout diagnosis by measuring monosodium urate crystal phagocytosis and quantitatively measured morphological differences between synthetic monosodium urate crystals and those found in synovial fluid[199]. Finally, recent studies using HT have identified diseases affecting the rheological properties of RBCs, as observed in metabolic diseases such as diabetes[110] and dyslipidaemia[200]. These studies highlight the potential for live cell-based drug discovery and disease diagnosis using HT in the future.

Reproducibility and data deposition

Reproducibility

HT imaging has relatively low variability during both the measurement and analysis because the measurement process does not alter or deteriorate the signal, unlike fluorescence imaging. This is because RI does not drastically change depending on the preparation, and HT measurements are carried out under a relatively low dose of illumination. Also, the analysis on HT images can be established in a relatively universal manner. RI is an endogenous physical property that does not require manual normalization, so each biological structure can be represented with unique patterns in the 3D RI image.

Despite inherent reproducibility of HT, achieving stable data acquisition entails meticulous attention to technical details. Variations in HT configurations — such as the illumination source wavelength, numerical apertures of the condenser and objective lenses and sensitivity of the image sensor — can significantly influence the resolution and SNR of 3D RI images. Moreover, the aberration in each implementation may result in hardware-specific artefacts that distort RI measurements or obscure structural details. Inspecting such variability among HT systems is also challenging as physical 3D phantoms for calibration purposes are scarce[201].

On another note, biological attributes derived from 3D RI images can be reproduced within a confirmed range of samples. That is, although RI is a consistent physical property, the patterns of specific structures can vary between and within species or depending on pathophysiological conditions. RBCs, for example, showcase notable differences: although typical human RBCs display cytoplasmic RI around 1.40 and lack a nucleus[202], amphibian RBCs were reported to have cytoplasmic RI near 1.351 and nuclear RI near 1.365 (ref. [

203]). In addition, a decrease in the cytoplasmic RI of human RBCs to approximately 1.37 was observed during malaria infection, indicating the digestion of haemoglobin by the parasites.

Data sharing

HT has the future potential for a multicentre database. Although the variability and difficulty in implementation are currently hindering factors, the consistency of light scattering ensures that HT measurements are reproducible and transparent. The recent commercialization of HT, by companies such as Tomocube and Nanolive, has spurred global studies adopting standardized HT measurements across various biomedical fields. Although creating a standard database is in its nascent stages, the burgeoning open research initiative is set to accelerate the expansion of HT research communities and advance data-driven HT analyses. Presently, HT data sets are shared via general repositories such as Figshare, Zenodo and Dryad, promoting open science principles. Best practices encourage sharing both raw and processed data, accompanied by comprehensive metadata to facilitate validation, reinterpretation and further research. Establishing minimum reporting standards for HT data, including detailed system configurations, sample preparations, imaging conditions and data processing details, is imperative for ensuring consistency, reproducibility and the advancement of HT research. These standards should include detailed descriptions of the HT system configuration (for example, wavelengths of the illumination source and the numerical aperture of the condenser and objective lenses), sample preparation methods, imaging conditions and data processing algorithms. Reporting the software version used for data analysis, along with any custom code or settings, further enhances reproducibility.

Limitations and optimizations

Artefacts in reconstruction

HT is not immune to artefacts that might degrade the HT image quality. This section highlights some common artefacts and suggests mitigation strategies (Fig. 7).

Fig. 7

Typical imaging artefacts in holotomography.

a, Coherent holotomography (HT) suffers from a distinct speckle noise caused by the undesired interference of light[204]. **b**, The noise arising from the imperfection of the illumination beam may deteriorate the hologram qualities for HT. **c**, The shot noise of photon measurement influences the reconstruction quality[49]. **d**, Sample-induced aberration reduces the reconstruction quality by breaking the weakly scattering assumption[50]. RI, refractive index; ROI, region of interest. Panel **a** adapted with permission from ref. [204], © Optica Publishing Group. Part **c** adapted with permission from ref. [49], © Optica Publishing Group. Panel **d** adapted with permission from ref. [50], © Optica Publishing Group.

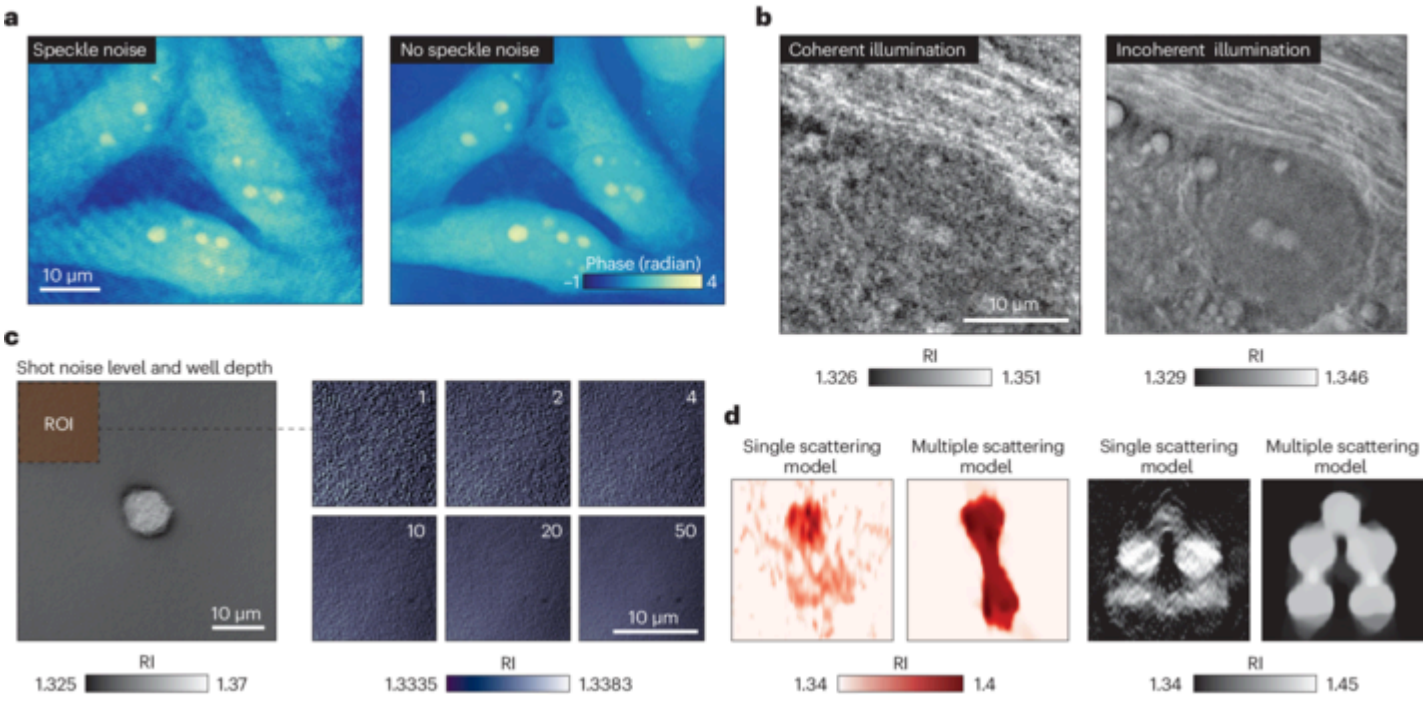

Coherent HT specifically faces noise issues resulting from the extended coherence length of laser illumination. These issues related to undesired diffraction by objects beside the sample, including the imperfection of the optical hardware and sample slide. Commonly, a wide range of factors are involved in the undesired diffraction, producing the speckle noise[204] (Fig. 7a). Hardware-oriented solutions are available for mitigating this coherent noise. One can reduce a significant portion of the coherent noise by ruling out multiple reflections within the beam splitter or from a protective glass shielding the camera. This involves aligning the angle of the beam splitter to prevent multiple reflections from entering the image sensor and replacing or removing the protective glass of the camera. Other countermeasures regarding hardware include maintaining an optical system free of dust and ensuring the spatial light modulator used for beam steering is properly calibrated. Computational solutions provide further mitigation of coherent noise, using shift-based differential phase retrieval[204] (Fig. 7a) and artificial intelligence-assisted noise removal[205, 206] (Supplementary Fig. 2d,e).

An effective remedy for the coherent noise issues is to switch to incoherent light for illumination[207] (Fig. 7b), yet other types of noise may persist. One class of the remaining noise is the camera shot noise (Fig. 7c), which naturally occurs during the Poisson process of detecting photons. Shot results in a pixelwise irregularity throughout the entire field of view of the reconstructed HT image. The shot noise can be mitigated by employing a camera with a larger full-well capacity and using more intense illumination[208].

Other elements of noise can be counteracted by considering the properties of the sample. For instance, when noise is absent in the background but evident within the sample, the culprit might be multiple scattering (Fig. 7d). In coherent HT, adjusting the phase unwrapping algorithm can help mitigate this challenge[209]. For scenarios in which extended reconstruction times are permissible, algorithms designed to counter multiple scattering can be employed to minimize related artefacts[50, 64, 65, 66, 67, 68]. Additionally, aligning the RI of a mounting medium with that of a sample stands as an effective strategy to curtail multiple scattering artefacts[210]. Employing low-coherence HT serves as an effective method to minimize multiple scattering artefacts, and it offers the advantage of rapid reconstruction as many artefacts are effectively averaged out[46]. However, when imaging samples with high scattering properties, there can be notable reductions in contrast and RI precision. In addition, if noise and diminished contrast predominantly manifest out of focus, virtual refocusing can serve as an effective solution[211], offering a balance with computational demands.

Large-sized HT images

Although advancements in optical engineering and image analysis are pushing HT towards accommodating larger data sets, there is still ground to cover. HT methodologies produce 3D images with subcellular resolution and expansive fields of view, capable of encompassing tissues and even entire slides. Yet, despite these strides in HT measurement techniques[8, 95], the potential of the derived images remains underutilized. The primary hindrances are the nascent understanding bridging large-scale HT images with their biomedical implications and the computational demands they introduce. Historically, studies involving extensive HT images have adopted a patch-based analysis, extrapolating individual patch data to span the entire image scale[14, 16, 212]. By dissecting and then piecing together, this strategy effectively localizes high-resolution features, culminating in a comprehensive field-of-view map drawn from these localized details.

Processing and analysing large-scale HT images necessitate advancements in computational strategies to fully harness their potential in biomedical research. These high-resolution 3D images, capturing extensive fields of view, offer unparalleled insights into tissue architecture and cellular dynamics, yet their biomedical implications are often not fully exploited owing to computational limitations and a gap in linking these images to specific biological contexts. Past research on established medical imaging modalities has showcased the feasibility of storing and profiling large-scale images, enabling global-scale attributes to be factored into analyses[213, 214]. Implementing compression algorithms could further enhance the handling of voluminous HT data. Although direct application of lossless compression algorithms is a possibility, efficient albeit lossy algorithms might be suitable if the information loss is negligible and does not compromise HT data precision[215]. By adopting and fine-tuning these computational approaches, the depth of information embedded in large-scale HT images will pave the way for novel insights.

To address these challenges, future research should aim at developing integrated analysis frameworks that can contextualize HT imaging data within the broader scope of biomedical research. This involves not just the processing of images for structural details but also the interpretation of these details to derive meaningful insights into health, disease progression and response to treatments. Efficient data management strategies, including the application of both lossless and selectively lossy compression algorithms, could facilitate the handling of large data volumes without sacrificing the precision of HT data. By enhancing computational methodologies to interpret large-scale HT images in relation to their biological significance, researchers can unlock new perspectives on cellular behaviour, disease pathology and therapeutic responses.

Outlook

Machine learning

Over the past decade, the advancement and proliferation of machine learning have reshaped imaging science, with HT being no exception. By integrating computer vision techniques into HT, intricate patterns that were previously elusive to manual or rule-based analyses have been discerned, ushering in a new era of biomedical applications.

A primary area of focus in integrating machine learning with HT has been the enhancement of the imaging process itself (Supplementary Fig. 2). More specifically, machine learning has been able to address both the limit of weak scattering approximation and the missing cone problem, with early works using deep neural networks as the platform for iterative RI reconstruction[64] (Supplementary Fig. 2a). In this study, the neural connectivity weights were fixed to mimic propagation through the sample, and the neural values corresponding to the RI were learned to satisfy the resulting intensity measurement. Beyond such utilization as an optical forward model, deep neural networks have been leveraged to secure HT image quality even on unknown data[63, 83, 205, 206, 216]. One way to do this is to replace the time-consuming and parameter-dependent regularization with a deep neural network. For example, a trained neural network was used to predict the image total variation regularized[71, 72, 73] from the initial HT reconstruction[83] (Supplementary Fig. 2b). Similarly, a different deep neural network trained with simulated data was able to counteract the resolution reduction originating from multiple scattering and the missing cone problem[63, 216]. Some studies have addressed the coherent HT-specific noise issue; for example, a neural network-based screening for noise-corrupted measurements applied before reconstruction effectively reduced noise in angle-scanning coherent HT[205]. Also, a deep neural network was constructed to yield a clear HT image when given a noisy HT image, by training in an unsupervised manner[206].

These machine learning approaches differ from the regularization techniques previously described in their learning aspect: although traditional regularization methods apply mathematical constraints based on previous knowledge (such as non-negativity and smoothness), machine-learning-based regularization and artefact removal adaptively learn these constraints from the data, potentially uncovering complex relationships that manual or rule-based techniques might miss. This adaptability makes machine learning an invaluable tool for enhancing HT imaging, leading to more precise and informative biomedical analyses.

Machine-learning the singular cell level-enhanced HT is making strides in the cell and tissue analysis by precisely discerning cell or tissue subtypes and physiological states. Traditional efforts relying on manual identification of biophysical properties often struggle with inherent variabilities among cells. However, with the integration of machine learning, especially deep learning, classification accuracy has substantially improved, allowing for precise differentiation of blood cells[160], immune cells[161, 217] and even bacteria[20] at the single-cell level. These advances promise substantial time and cost efficiencies in laboratory diagnostics. Moreover, machine-learning-driven advancements in HT are bridging the gap of molecular specificity by infusing RI contrast with detailed molecular profiles, enabling predictions based on morphological indicators present in HT imagery[11, 14]. This approach offers benefits such as reduced cellular disruptions, accelerated data capture and expanded imaging channels. Although initial focus has centred around singular cells, expanding to tissues and 3D cultures is crucial for deeper insights into cellular behaviour. Integrating machine learning with HT in the histopathological analysis of tissue slides and probing 3D cultures holds great promise for enriching biomedical research and understanding living cells in their native environments.

Enhancing existing applications

Histology

HT has shown unique advantages in histological applications[218] as a consistent and streamlined 3D imaging platform that abolishes the need for labour-intensive staining and preparation[8]. With rapid imaging speeds, HT surpasses other label-free modalities which often are limited by scanning geography and low SNRs[219]. HT is consistent, ensuring standardized analysis protocols. With its 3D analytical capabilities, HT goes beyond traditional 2D assessments, revealing detailed multiscale structures across various tissue types[8] (Supplementary Fig. 3). Heterogeneity analyses of HT images pinpoint malignant areas on standard histology slides of renal cell carcinoma, underscoring its clinical promise[16]. HT can also be applied to 3D tumour models in patients with gastric cancer undergoing immunotherapy, revealing spatial organization and heterogeneous interactions of various cellular and non-cellular components in the tissue (Fig. 8). Through the integration of artificial intelligence algorithms and spatial molecular technologies, HT becomes a powerful tool for identifying and evaluating tissue-level biomarkers and therapeutic targets within the tissue microenvironment. Despite lower specificity in pinpointing individual subcellular functions, strategies such as assessing the statistical distribution of tissue RI[220, 221] and leveraging artificial intelligence to simulate staining processes[222] have been used to infer tissue type or detect disease and to improve diagnostics. Artificial intelligence interpretation of RI metrics enables swifter and more precise diagnostic conclusions.

Fig. 8

Artificial-intelligence-assisted holotomography for investigating the organization of a 3D tissue.

a, A cropped region of a histopathology tissue imaged after H&E staining (corresponds to a 256 × 256 region from a standard 40× histology image). **b**, The corresponding holotomography (HT) images of the identical field of view of the tissue (each column illustrates a different axial section of the 5-µm-thick tissue). **c**, Artificial-intelligence-driven identification and segmentation of cellular and non-cellular tissue substructures, for the HT section images of part **b**. **d**, Artificial-intelligence-assisted detection of collagen, along with the analysis of collagen fibre arrangement and alignment derived from the HT section images of part **b**. **e**, Volumetric rendering of the tissue segmentation in part **c**, merged into a 3D structure. H&E, haematoxylin and eosin.

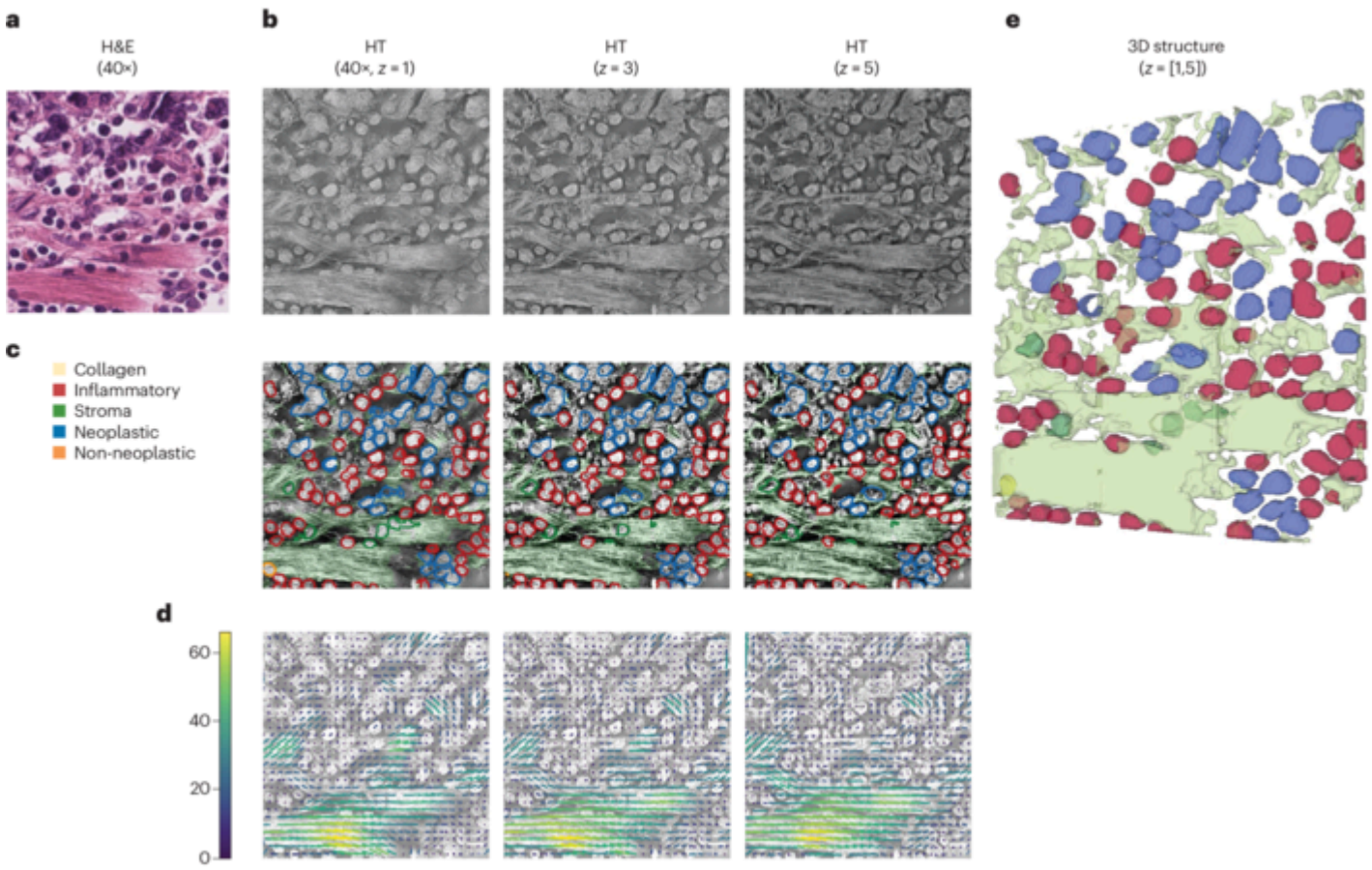

Three-dimensional biology

Exploring biological systems in 3D contexts more accurately mirrors in vivo conditions. Although the utility of HT in organoid studies is palpable, there is room for advancement, such as tailoring HT for high-throughput applications, necessitating swifter image acquisition [illegible] multiple organoids. Optimization of conditions for monitoring robust densely packed samples — such as brain organoids — in live circumstances is needed. This includes harnessing in vivo clearing methods[223] or fine-tuning imaging

conditions. An on-going issue in examining organoids is the limited penetration depth of HT imaging; the foundational principle of HT, anchored in the inversion of light scattering and presupposing single scattering within samples, curtails its imaging depth to a mere handful of cell layers. By melding HT with incoherent light sources, this reach has been extended to ~100–150 µm. Yet, environments conducive to high-fidelity imaging remain bound within the 50 µm threshold, hemmed in by multifaceted light scattering and sample-induced distortions[7]. This is particularly challenging given that standard organoid dimensions span from 100 µm to 1 mm. The advent of artificial-intelligence-driven computational tools designed for visual amplification and noise reduction can further illuminate deep organoid structures, and novel iterative algorithms are able to enhance depth penetration[15]. As HT continues to adapt, addressing both multiple light scattering and sample-induced distortions[50], its potency in organoid research and its utility in drug screening are set to ascend.

Regenerative medicine

Applying HT imaging to PSC biology presents challenges owing to the need for advanced analyses for colony-like growth, variations in pluripotency and differentiation influenced by genetic/epigenetic factors and culture conditions and the resulting heterogeneous cultures during somatic cell reprogramming. Precise high-resolution multiplexed microtomography of diverse PSC lines will enhance the accuracy and applicability of label-free image-based quality control of PSCs. The automation of image analysis and the scalability of HT imaging systems are expected to address the complexities of applying HT imaging to PSC biology. Advances in automated image analysis through the integration of machine learning will transform the accurate identification, classification and tracking of nuanced changes in pluripotency and differentiation stages of PSCs and will minimize manual analysis, reduce biases and facilitate the processing of large data sets with unprecedented speed and accuracy. Furthermore, enhancements in HT imaging technology are anticipated to improve sample handling and throughput capabilities for PSC cultures, speeding up the screening of genetic and epigenetic factors and establishing culture conditions that promote optimal growth and differentiation. These forecasted advances in HT for the surveillance and improvement of reprogramming of hPSCs and cellular differentiation hold enormous potential to improve our understanding of stem cell biology and provide promising methodologies for safe and cost-efficient clinical cell therapy.

In vitro fertilization

A non-invasive, high-speed 3D imaging modality is needed to quantitatively analyse the 3D morphokinetics of freely moving sperm used in IVF. Although oocytes have not received as much attention as embryos and sperm[55], accurately predicting their developmental potential before IVF treatment could greatly simplify and streamline the process of achieving a successful pregnancy. The limited focus on oocytes compared with embryos and sperm in IVF-related research likely stems from a combination of technical challenges and historical oversight. Technically, oocytes present unique imaging challenges owing to their size, optical properties and the need to maintain their viability during analysis. Oocytes are significantly larger than sperm, requiring imaging techniques that can capture their entire volume without compromising resolution or causing damage. Additionally, the dense, opaque nature of the zona pellucida (the outer layer of the oocyte) can hinder optical clarity, necessitating imaging modalities capable of penetrating this layer without affecting oocyte developmental potential. This kind of evaluation of oocytes became more important as oocyte cryopreservation for future use became a routine clinical practice in reproductive medicine.

Notably, combining HT with machine learning can be a promising route for the accurate and automatic segmentation of good-quality oocytes and sperm[224]. Given the high spatiotemporal resolution and data reproducibility, it also has the potential to serve as a time-lapse monitoring system for continuously monitoring embryo development[225], improving the accuracy in machine-learning-assisted selection of embryos with higher potential to achieve pregnancy and live birth[226, 227].

Conclusion

The precision, adaptability and label-free imaging and quantitative analysis potential of HT in elucidating intricate biological phenomena, from the cellular to the organoid level, portends a future in which we can observe and understand processes of life with an unprecedented depth and clarity. Furthermore, insights and techniques of other disciplines will foster new avenues for HT to contribute, while remedying the limitations such as the missing cone problem, imaging depth, multiple scattering and marginal molecular specificity. The integration of HT with complementary techniques, including machine learning and other advanced imaging modalities, is addressing many of the current limitations of HT. Furthermore, as HT becomes more accessible and integrated into mainstream research, its applications will undoubtedly extend beyond the laboratory, impacting clinical diagnostics, therapeutic development and patient care.

Supplementary information

The online version contains supplementary material available at https://doi.org/10.1038/s43586-024-00327-1.

Publisher's note Springer Nature remains neutral with regard to jurisdictional claims in published maps and institutional affiliations.

Acknowledgements

This work was supported by the National Research Foundation of Korea (2015R1A3A2066550, 2022M3H4A1A02074314), Institute for Information and Communications Technology Planning and Evaluation (IITP; 2021-0-00745) grant funded by the Ministry of Science and ICT, Republic of Korea, the Korea Health Technology R&D Project through the Korea Health Industry Development Institute, funded by the Ministry of Health and Welfare, Republic of Korea (HI21C0977, HR22C1605), Basic Science Research Program through the National Research Foundation of Korea funded by the Ministry of Education, Republic of Korea (RS-2023-00241278).

Author contributions

Introduction (Y.K.P. and G.K.); Experimentation (Y.K.P. and H.H.); Results (Y.K.P., G.K., H.H., K.K., J.-H.L., S.S.L., J.H., C.L., H.P., K.-J.Y., Y.S., G.S., I.H., L.M., J.H.K., T.H.H., S.L., P.O., B.-K.K. and J.G.); Applications (Y.K.P., G.K., K.K., J.-H.L., S.S.L., J.H., C.L., H.P.,

K.-J.Y., Y.S., G.S., I.H., L.M., J.H.K., T.H.H., S.L., P.O., B.-K.K. and J.G.); Reproducibility and data deposition (Y.K.P. and G.K.); Limitations and optimizations (Y.K.P. and H.H.); Outlook (Y.K.P. and G.K.); Overview of the Primer (Y.K.P.).

Peer review

Peer review information

Nature Reviews Methods Primers thanks Kevin Tsia, Thomas Zangle and the other, anonymous, reviewer(s) for their contribution to the peer review of this work.

Competing interests

H.H., K.K. and Y.K.P. have financial interests in Tomocube Inc., a company that commercializes holotomography instruments.

Glossary

Biomolecular condensates
Membrane-less assemblies of proteins and nucleic acids, characterized by inhomogeneous, non-stoichiometric molecular arrangements, encompassing structures such as nucleoli, nuclear speckles, heterochromatin, cytoplasmic stress granules, germ granules and others.
Coherent HT
A HT technique that uses a coherent light source such as a laser for angle-scanned illumination.
Coherent light illumination
Light with well-defined propagation angle which can be described by a plane wave.
Fourier diffraction theorem
A theorem which states that the Fourier transform of the aperture function of an object is proportional to the far-field diffraction pattern, linking the spatial domain with the frequency domain and enabling the reconstruction of 3D RI tomogram via the analysis inverse wave scattering and propagation.
Kramers–Kronig relations
A fundamental principle in physics that describes the relationship between the real and imaginary parts of a complex function, used in holotomography to retrieve phase information from intensity measurements.
Lipid droplets
Subcellular organelles primarily involved in the storage and regulation of lipids, serving as energy reservoirs and playing a role in cellular lipid metabolism and signalling pathways within cells.
Mach–Zehnder interferometric techniques
Optical techniques that split a laser beam into two distinct paths, which are then recombined to form interference patterns, providing an optical field with detailed amplitude and phase information.
Missing cone problem
The issue in tomographic imaging in which certain angles cannot be sampled owing to geometric or physical constraints, resulting in a loss of information and potentially leading to inaccuracies in the reconstructed images.
Non-negativity
In regularization algorithms addressing the missing cone problem, the non-negativity is a constraint applied during reconstruction that ensures all predicted values for the missing data are greater than or equal to zero.
Refractive index
A dimensionless number given by the ratio of speed of light in a medium to that in vacuum.
Spatially low-coherence HT
A HT technique that exploits spatially low-coherent light source for illumination and axially scans the sample.
Temporally low-coherence HT
A HT technique that exploits temporally low-coherent light sources such as LED for angle-scanned illumination.

Supplementary information

Supplementary Information

References

1. Robertson, L. A. van Leeuwenhoek microscopes — where are they now? *FEMS Microbiol. Lett.* **362**, fnv056 (2015).

2. Wiedenmann, J., Oswald, F. & Nienhaus, G. U. Fluorescent proteins for live cell imaging: opportunities, limitations, and challenges. *IUBMB Life* **61**, 1029–1042 (2009).

3. Ghosh, B. & Agarwal, K. Viewing life without labels under optical microscopes. *Commun. Biol.* **6**, 559 (2023).

4. Shaked, N. T., Boppart, S. A., Wang, L. V. & Popp, J. Label-free biomedical optical imaging. *Nat. Photon.* **17**, 1031–1041 (2023).

5. Park, Y., Depeursinge, C. & Popescu, G. Quantitative phase imaging in biomedicine. *Nat. Photon.* **12**, 578–589 (2018).

6. Ledwig, P. & Robles, F. E. Epi-mode tomographic quantitative phase imaging in thick scattering samples. *Biomed. Opt. Express* **10**, 3605–3621 (2019).

7. Lee, M. J. et al. Long-term three-dimensional high-resolution imaging of live unlabeled small intestinal organoids using low-coherence holotomography. Preprint at *bioRxiv* https://doi.org/10.1101/2023.09.16.558039 AQ9 (2023).

8. Hugonnet, H. et al. Multiscale label-free volumetric holographic histopathology of thick-tissue slides with subcellular resolution. *Adv. Photon.* **3**, 026004 (2021).

9. Merola, F. et al. Tomographic flow cytometry by digital holography. *Light Sci. Appl.* **6**, e16241 (2017).

10. Sung, Y. et al. Three-dimensional holographic refractive-index measurement of continuously flowing cells in a microfluidic channel. *Phys. Rev. Appl.* **1**, 014002 (2014).

11. Pirone, D. et al. Stain-free identification of cell nuclei using tomographic phase microscopy in flow cytometry. *Nat. Photon.* **16**, 851–859 (2022).

12. Lee, C. et al. Label-free three-dimensional observations and quantitative characterisation of on-chip vasculogenesis using optical diffraction tomography. *Lab Chip* **21**, 494–501 (2021).

13. Tebon, P. J. et al. Drug screening at single-organoid resolution via bioprinting and interferometry. *Nat. Commun.* **14**, 3168 (2023).

14. Jo, Y. et al. Label-free multiplexed microtomography of endogenous subcellular dynamics using generalizable deep learning. *Nat. Cell Biol.* **23**, 1329–1337 (2021).

15. Yasuhiko, O. & Takeuchi, K. In-silico clearing approach for deep refractive index tomography by partial reconstruction and wave-backpropagation. *Light Sci. Appl.* **12**, 101 (2023).

16. Park, J. et al. Quantification of structural heterogeneity in H&E stained clear cell renal cell carcinoma using refractive index tomography. *Biomed. Opt. Express* **14**, 1071–1081 (2023).

17. Lee, A. J. et al. Label-free monitoring of 3D cortical neuronal growth in vitro using optical diffraction tomography. *Biomed. Opt. Express* **12**, 6928–6939 (2021).

18. Wang, Z. et al. Spatial light interference tomography (SLIT). *Opt. Express* **19**, 19907–19918 (2011).

19. Oh, J. et al. Three-dimensional label-free observation of individual bacteria upon antibiotic treatment using optical diffraction tomography. *Biomed. Opt. Express* **11**, 1257–1267 (2020).

20. Kim, G. et al. Rapid species identification of pathogenic bacteria from a minute quantity exploiting three-dimensional quantitative phase imaging and artificial neural network. *Light Sci. Appl.* **11**, 190 (2022).

21. Wolf, E. Three-dimensional structure determination of semi-transparent objects from holographic data. *Opt. Commun.* **1**, 153–156 (1969).

22. Kak, A. C. & Slaney, M. *Principles of Computerized Tomographic Imaging* (SIAM, 2001).

23. Takeda, M., Ina, H. & Kobayashi, S. Fourier-transform method of fringe-pattern analysis for computer-based topography and interferometry. *J. Opt. Soc. Am.* **72**, 156–160 (1982).

24. Yamaguchi, I. & Zhang, T. Phase-shifting digital holography. *Opt. Lett.* **22**, 1268–1270 (1997).

25. Kim, K. et al. Diffraction optical tomography using a quantitative phase imaging unit. *Opt. Lett.* **39**, 6935–6938 (2014).

26. Zdańkowski, P. et al. Common-path intrinsically achromatic optical diffraction tomography. *Biomed. Opt. Express* **12**, 4219–4234 (2021).

27. Kim, Y. et al. Common-path diffraction optical tomography for investigation of three-dimensional structures and dynamics of biological cells. *Opt. Express* **22**, 10398–10407 (2014).

28. Bon, P., Maucort, G., Wattellier, B. & Monneret, S. Quadriwave lateral shearing interferometry for quantitative phase microscopy of living cells. *Opt. Express* **17**, 13080–13094 (2009).

29. Baek, Y. & Park, Y. Intensity-based holographic imaging via space-domain Kramers–Kronig relations. *Nat. Photon.* **15**, 354–360 (2021).

30. Ling, R., Tahir, W., Lin, H.-Y., Lee, H. & Tian, L. High-throughput intensity diffraction tomography with a computational microscope. *Biomed. Opt. Express* **9**, 2130–2141 (2018).

31. Gbur, G. & Wolf, E. Hybrid diffraction tomography without phase information. *J. Opt. Soc. Am. A* **19**, 2194–2202 (2002).

32. Lee, J. et al. High-precision and low-noise dielectric tensor tomography using a micro-electromechanical system mirror. Preprint at https://arxiv.org/abs/2402.09070 (2024). AQ10

33. Choi, W. et al. Tomographic phase microscopy. *Nat. Methods* **4**, 717–719 (2007).

34. Lauer, V. New approach to optical diffraction tomography yielding a vector equation of diffraction tomography and a novel tomographic microscope. *J. Microsc.* **205**, 165–176 (2002).

35. Kim, K. et al. High-resolution three-dimensional imaging of red blood cells parasitized by *Plasmodium falciparum* and in situ hemozoin crystals using optical diffraction tomography. *J. Biomed. Opt.* **19**, 011005 (2014).

36. Park, C., Lee, K., Baek, Y. & Park, Y. Low-coherence optical diffraction tomography using a ferroelectric liquid crystal spatial light modulator. *Opt. Express* **28**, 39649–39659 (2020).

37. Shin, S., Kim, K., Yoon, J. & Park, Y. Active illumination using a digital micromirror device for quantitative phase imaging. *Opt. Lett.* **40**, 5407–5410 (2015).

38. Charrière, F. et al. Cell refractive index tomography by digital holographic microscopy. *Opt. Lett.* **31**, 178–180 (2006).

39. Habaza, M., Gilboa, B., Roichman, Y. & Shaked, N. T. Tomographic phase microscopy with 180 rotation of live cells in suspension by holographic optical tweezers. *Opt. Lett.* **40**, 1881–1884 (2015).

40. Lee, K., Shin, S., Yaqoob, Z., So, P. T. C. & Park, Y. Low-coherent optical diffraction tomography by angle-scanning illumination. *J. Biophotonics* **12**, e201800289 (2019).

41. Streibl, N. Three-dimensional imaging by a microscope. *J. Opt. Soc. Am. A* **2**, 121–127 (1985).

42. Chen, M., Tian, L. & Waller, L. 3D differential phase contrast microscopy. *Biomed. Opt. Express* **7**, 3940–3950 (2016).

43. Hugonnet, H., Lee, M. & Park, Y. Optimizing illumination in three-dimensional deconvolution microscopy for accurate refractive index tomography. *Opt. Express* **29**, 6293–6301 (2021).

44. Soto, J. M., Rodrigo, J. A. & Alieva, T. Label-free quantitative 3D tomographic imaging for partially coherent light microscopy. *Opt. Express* **25**, 15699–15712 (2017).

45. Kim, T. et al. White-light diffraction tomography of unlabelled live cells. *Nat. Photon.* **8**, 256–263 (2014).

46. Nguyen, T. H., Kandel, M. E., Rubessa, M., Wheeler, M. B. & Popescu, G. Gradient light interference microscopy for 3D imaging of unlabeled specimens. *Nat. Commun.* **8**, 210 (2017).

47. Li, J. et al. Transport of intensity diffraction tomography with non-interferometric synthetic aperture for three-dimensional label-free microscopy. *Light Sci. Appl.* **11**, 154 (2022).

48. Phillips, Z. F., Chen, M. & Waller, L. Single-shot quantitative phase microscopy with color-multiplexed differential phase contrast (cDPC). *PLoS ONE* **12**, e0171228 (2017).

49. Lee, C. et al. Single-shot refractive index slice imaging using spectrally multiplexed optical transfer function reshaping. Preprint at https://arxiv.org/abs/2301.05425 AQ11 (2023).

50. Lee, M., Hugonnet, H. & Park, Y. Inverse problem solver for multiple light scattering using modified Born series. *Optica* **9**, 177–182 (2022).

51. Yasuhiko, O., Takeuchi, K., Yamada, H. & Ueda, Y. Multiple-scattering suppressive refractive index tomography for the label-free qua ntitative assessment of multicellular spheroids. *Biomed. Opt. Express* **13**, 962–979 (2022).

52. Bruning, J. H. et al. Digital wavefront measuring interferometer for testing optical surfaces and lenses. *Appl. Opt.* **13**, 2693–2703 (197 4).

53. Born, M. & Wolf, E. *Principles of Optics*: *Electromagnetic Theory of Propagation, Interference and Diffraction of Light* 7th edn (Ca mbridge Univ. Press, 1999).

54. Sung, Y. et al. Optical diffraction tomography for high resolution live cell imaging. *Opt. Express* **17**, 266–277 (2009).

55. Rienzi, L., Vajta, G. & Ubaldi, F. Predictive value of oocyte morphology in human IVF: a systematic review of the literature. *Hum. Re prod. Update* **17**, 34–45 (2010).

56. Novotny, L. & Hecht, B. *Principles of Nano-Optics* (Cambridge Univ. Press, 2012).

57. Shin, S. et al. Tomographic measurement of dielectric tensors at optical frequency. *Nat. Mater.* **21**, 317–324 (2022).

58. Saba, A., Lim, J., Ayoub, A. B., Antoine, E. E. & Psaltis, D. Polarization-sensitive optical diffraction tomography. *Optica* **8**, 402–408 (2021).

59. Yeh, L.-H. et al. *Novel Techniques in Microscopy* NM3C.4 (Optica Publishing Group).

60. Jenkins, M. H. & Gaylord, T. K. Three-dimensional quantitative phase imaging via tomographic deconvolution phase microscopy. *Ap pl. Opt.* **54**, 9213–9227 (2015).

61. Hugonnet, H., Lee, M. J. & Park, Y. K. Quantitative phase and refractive index imaging of 3D objects via optical transfer function res haping. *Opt. Express* **30**, 13802–13809 (2022).

62. Bon, P., Aknoun, S., Monneret, S. & Wattellier, B. Enhanced 3D spatial resolution in quantitative phase microscopy using spatially in coherent illumination. *Opt. Express* **22**, 8654–8671 (2014).

63. Lim, J., Ayoub, A. B., Antoine, E. E. & Psaltis, D. High-fidelity optical diffraction tomography of multiple scattering samples. *Light: Sci. Appl.* **8**, 82 (2019).

64. Kamilov, U. S. et al. Learning approach to optical tomography. *Optica* **2**, 517–522 (2015).

65. Pham, T.-A. et al. Versatile reconstruction framework for diffraction tomography with intensity measurements and multiple scattering. *Opt. Express* **26**, 2749–2763 (2018).

66. Chen, M., Ren, D., Liu, H.-Y., Chowdhury, S. & Waller, L. Multi-layer born multiple-scattering model for 3D phase microscopy. *Opti ca* **7**, 394–403 (2020).

67. Soubies, E., Pham, T.-A. & Unser, M. Efficient inversion of multiple-scattering model for optical diffraction tomography. *Opt. Expres s* **25**, 21786–21800 (2017).

68. Hugonnet, H., Lee, M., Shin, S. & Park, Y. Vectorial inverse scattering for dielectric tensor tomography: overcoming challenges of rec onstruction of highly scattering birefringent samples. *Opt. Express* **31**, 29654–29663 (2023).

69. Lim, J. et al. Comparative study of iterative reconstruction algorithms for missing cone problems in optical diffraction tomography. *O pt. Express* **23**, 16933–16948 (2015).

70. Gerchberg, R. Super-resolution through error energy reduction. *Opt. Acta Int. J. Opt.* **21**, 709–720 (1974).

71. LaRoque, S. J., Sidky, E. Y. & Pan, X. Accurate image reconstruction from few-view and limited-angle data in diffraction tomograph y. *J. Opt. Soc. Am. A* **25**, 1772–1782 (2008).

72. Lustig, M., Donoho, D. & Pauly, J. M. Sparse MRI: the application of compressed sensing for rapid MR imaging. *Magn. Reson. Med.* **58**, 1182–1195 (2007).

73. Rudin, L. I., Osher, S. & Fatemi, E. Nonlinear total variation based noise removal algorithms. *Phys. D Nonli. Phenom.* **60**, 259–268 (1992).

74. Lefkimmiatis, S., Ward, J. P. & Unser, M. Hessian Schatten-norm regularization for linear inverse problems. *IEEE Trans. Image Process.* **22**, 1873–1888 (2013).

75. Pham, T.-A et al. Three-dimensional optical diffraction tomography with Lippmann–Schwinger model. *IEEE Trans. Comput. Imaging* **6**, 727–738 (2020).

76. Delaney, A. H. & Bresler, Y. Globally convergent edge-preserving regularized reconstruction: an application to limited-angle tomography. *IEEE Trans. Image Process.* **7**, 204–221 (1998).

77. Sung, Y., Choi, W., Lue, N., Dasari, R. R. & Yaqoob, Z. Stain-free quantification of chromosomes in live cells using regularized tomographic phase microscopy. *PLoS ONE* **7**, e49502 (2012).

78. Charbonnier, P., Blanc-Féraud, L., Aubert, G. & Barlaud, M. Deterministic edge-preserving regularization in computed imaging. *IEEE Trans. Image Process.* **6**, 298–311 (1997).

79. Krauze, W. Optical diffraction tomography with finite object support for the minimization of missing cone artifacts. *Biomed. Opt. Express* **11**, 1919–1926 (2020).

80. Hugonnet, H., Shin, S. & Park, Y. Regularization of dielectric tensor tomography. *Opt. Express* **31**, 3774–3783 (2023).

81. Chung, H., Huh, J., Kim, G., Park, Y. K. & Ye, J. C. Missing cone artifact removal in ODT using unsupervised deep learning in the projection domain. *IEEE Trans. Comput. Imaging* **7**, 747–758 (2021).

82. Zhou, K. C. & Horstmeyer, R. Diffraction tomography with a deep image prior. *Opt. Express* **28**, 12872–12896 (2020).

83. Ryu, D. et al. DeepRegularizer: rapid resolution enhancement of tomographic imaging using deep learning. *IEEE Trans. Med. Imaging* **40**, 1508–1518 (2021).

84. Yang, F., Pham, T.-A, Gupta, H., Unser, M. & Ma, J. Deep-learning projector for optical diffraction tomography. *Opt. Express* **28**, 3905–3921 (2020).

85. Tam, K. C. & Perez-Mendez, V. Tomographical imaging with limited-angle input. *J. Opt. Soc. Am.* **71**, 582–592 (1981).

86. Medoff, B. P., Brody, W. R., Nassi, M. & Macovski, A. Iterative convolution backprojection algorithms for image reconstruction from limited data. *J. Opt. Soc. Am.* **73**, 1493–1500 (1983).

87. McNally, J. G., Preza, C., Conchello, J.-A. & Thomas, L. J. Artifacts in computational optical-sectioning microscopy. *J. Opt. Soc. Am. A* **11**, 1056–1067 (1994).

88. Andersen, A. H. & Kak, A. C. Simultaneous algebraic reconstruction technique (SART): a superior implementation of the art algorithm. *Ultrason. Imaging* **6**, 81–94 (1984).

89. Midgley, P. A. & Weyland, M. 3D electron microscopy in the physical sciences: the development of *Z*-contrast and EFTEM tomography. *Ultramicroscopy* **96**, 413–431 (2003).

90. Moser, S., Jesacher, A. & Ritsch-Marte, M. Efficient and accurate intensity diffraction tomography of multiple-scattering samples. *Opt. Express* **31**, 18274–18289 (2023).

91. Xu, J., Zhao, Y., Li, H. & Zhang, P. An image reconstruction model regularized by edge-preserving diffusion and smoothing for limited-angle computed tomography. *Inverse Probl.* **35**, 085004 (2019).

92. Chen, M., Mi, D., He, P., Deng, L. & Wei, B. A CT reconstruction algorithm based on L 1/2 regularization. *Comput. Math. Methods Med*. **2014** AQ12 (2014).

93. Yu, W. & Zeng, L. ℓ0 gradient minimization based image reconstruction for limited-angle computed tomography. *PLoS ONE* **10**, e0130793 (2015).

94. Deng, X., Liu, X. & Li, H. In *Proceedings of the Third International Symposium on Image Computing and Digital Medicine* 182–186. AQ13

95. Zuo, C., Sun, J., Li, J., Asundi, A. & Chen, Q. Wide-field high-resolution 3D microscopy with Fourier ptychographic diffraction tomography. *Opt. Lasers Eng.* **128**, 106003 (2020).

96. Horstmeyer, R., Chung, J., Ou, X., Zheng, G. & Yang, C. Diffraction tomography with Fourier ptychography. *Optica* **3**, 827–835 (2016).

97. Syga, Ł., Spakman, D., Punter, C. M. & Poolman, B. Method for immobilization of living and synthetic cells for high-resolution imaging and single-particle tracking. *Sci. Rep.* **8**, 1–12 (2018).

98. Lee, P. J., Helman, N. C., Lim, W. A. & Hung, P. J. A microfluidic system for dynamic yeast cell imaging. *Biotechniques* **44**, 91–95 (2008).

99. Lee, S. S., Vizcarra, I. A., Huberts, D. H., Lee, L. P. & Heinemann, M. Whole lifespan microscopic observation of budding yeast aging through a microfluidic dissection platform. *Proc. Natl Acad. Sci. USA* **109**, 4916–4920 (2012).

100. Shin, J., Kim, G., Park, J., Lee, M. & Park, Y. Long-term label-free assessments of individual bacteria using three-dimensional quantitative phase imaging and hydrogel-based immobilization. *Sci. Rep.* **13**, 46 (2023).

101. Peddie, C. J. et al. Volume electron microscopy. *Nat. Rev. Methods Primers* **2**, 51 (2022).

102. Li, D. et al. Extended-resolution structured illumination imaging of endocytic and cytoskeletal dynamics. *Science* **349**, aab3500 (2015).

103. Seifert, T. S. et al. Longitudinal and transverse electron paramagnetic resonance in a scanning tunneling microscope. *Sci. Adv.* **6**, eabc5511 (2020).

104. Jensen, E. C. Use of fluorescent probes: their effect on cell biology and limitations. *Anat. Rec.* **295**, 2031–2036 (2012).

105. Kim, K. et al. Optical diffraction tomography techniques for the study of cell pathophysiology. *J. Biomed. Photon. Eng.* **2**, 020201 (2016).

106. Elmer-Dixon, M. M. & Bowler, B. E. Rapid quantification of vesicle concentration for DOPG/DOPC and cardiolipin/DOPC mixed lipid systems of variable composition. *Anal. Biochem.* **553**, 12–14 (2018).

107. Tasic, A. Z., Djordjevic, B. D., Grozdanic, D. K. & Radojkovic, N. Use of mixing rules in predicting refractive indexes and specific refractivities for some binary liquid mixtures. *J. Chem. Eng. Data* **37**, 310–313 (1992).

108. Kim, K. et al. Three-dimensional label-free imaging and quantification of lipid droplets in live hepatocytes. *Sci. Rep.* **6**, 36815 (2016).

109. José, A. R., Juan, M. S. & Tatiana, A. In *Proc. SPIE*. 1106016. AQ14

110. Lee, S. et al. Refractive index tomograms and dynamic membrane fluctuations of red blood cells from patients with diabetes mellitus. *Sci. Rep.* **7**, 1039 (2017).

111. Pachitariu, M. & Stringer, C. Cellpose 2.0: how to train your own model. *Nat. Methods* **19**, 1634–1641 (2022).

112. Ma, J. et al. Segment anything in medical images. *Nat. Commun.* **15**, 654 (2024).

113. Berg, S. et al. ilastik: interactive machine learning for (bio) image analysis. *Nat. Methods* **16**, 1226–1232 (2019).

114. Barer, R. & Tkaczyk, S. Refractive index of concentrated protein solutions. *Nature* **173**, 821–822 (1954).

nd interferometry of living cells. *J. Opt. Soc. Am.* **47**, 545–556 (1957).

116. Lee, S. Y., Park, H. J., Best-Popescu, C., Jang, S. & Park, Y. K. The effects of ethanol on the morphological and biochemical properties of individual human red blood cells. *PLoS ONE* **10**, e0145327 (2015).

117. Hur, J., Kim, K., Lee, S., Park, H. & Park, Y. Melittin-induced alterations in morphology and deformability of human red blood cells using quantitative phase imaging techniques. *Sci. Rep.* **7**, 9306 (2017).

118. Lee, H. J., Lee, S., Park, H., Park, Y. & Shin, J. Three-dimensional shapes and cell deformability of rat red blood cells during and after asphyxial cardiac arrest. *Emerg. Med. Int*. **2019** (2019).

119. Choi, S. Y., Oh, J., Jung, J., Park, Y. & Lee, S. Y. Three-dimensional label-free visualization and quantification of polyhydroxyalkanoates in individual bacterial cell in its native state. *Proc. Natl Acad. Sci. USA* **118**, e2103956118 (2021).

120. Park, C., Shin, S. & Park, Y. Generalized quantification of three-dimensional resolution in optical diffraction tomography using the projection of maximal spatial bandwidths. *J. Opt. Soc. Am. A* **35**, 1891–1898 (2018).

121. Schürmann, M. et al. Three-dimensional correlative single-cell imaging utilizing fluorescence and refractive index tomography. *J. Biophotonics* **11**, e201700145 (2018).

122. Kim, K. & Guck, J. The relative densities of cytoplasm and nuclear compartments are robust against strong perturbation. *Biophys. J.* **119**, 1946–1957 (2020).

123. Bakhshandeh, S. et al. Optical quantification of intracellular mass density and cell mechanics in 3D mechanical confinement. *Soft Matter* **17**, 853–862 (2021).

124. Roffay, C. et al. Passive coupling of membrane tension and cell volume during active response of cells to osmosis. *Proc. Natl Acad. Sci. USA* **118**, e2103228118 (2021).

125. Yoon, J. et al. Label-free characterization of white blood cells by measuring 3D refractive index maps. *Biomed. Opt. Express* **6**, 3865–3875 (2015).

126. Banani, S. F., Lee, H. O., Hyman, A. A. & Rosen, M. K. Biomolecular condensates: organizers of cellular biochemistry. *Nat. Rev. Mol. Cell Biol.* **18**, 285–298 (2017).

127. Shin, Y. & Brangwynne, C. P. Liquid phase condensation in cell physiology and disease. *Science* **357**, eaaf4382 (2017).

128. Kim, T.-K., Lee, B.-W., Fujii, F., Kim, J. K. & Pack, C.-G. Physicochemical properties of nucleoli in live cells analyzed by label-free optical diffraction tomography. *Cells* **8**, 699 (2019).

129. Kim, Y. et al. Characterizing organelles in live stem cells using label-free optical diffraction tomography. *Mol. Cell* **44**, 851 (2021).

130. Kim, T.-K. et al. Mitotic chromosomes in live cells characterized using high-speed and label-free optical diffraction tomography. *Cells* **8**, 1368 (2019).

131. Biswas, A., Kim, K., Cojoc, G., Guck, J. & Reber, S. The *Xenopus* spindle is as dense as the surrounding cytoplasm. *Dev. Cell* **56**, 967–975.e5 (2021).

132. Sandoz, P. A., Tremblay, C., van der Goot, F. G. & Frechin, M. Image-based analysis of living mammalian cells using label-free 3D refractive index maps reveals new organelle dynamics and dry mass flux. *PLoS Biol.* **17**, e3000553 (2019).

133. Dong, D. et al. Super-resolution fluorescence-assisted diffraction computational tomography reveals the three-dimensional landscape of the cellular organelle interactome. *Light Sci. Appl.* **9**, 11 (2020).

134. Kim, K. et al. Correlative three-dimensional fluorescence and refractive index tomography: bridging the gap between molecular specificity and quantitative bioimaging. *Biomed. Opt. Express* **8**, 5688–5697 (2017).

135. Simon, B., Debailleul, M., Beghin, A., Tourneur, Y. & Haeberlé, O. High-resolution tomographic diffractive microscopy of biological samples. *J. Biophoton.* **3**, 462–467 (2010).

136. Chowdhury, S., Eldridge, W. J., Wax, A. & Izatt, J. A. Structured illumination microscopy for dual-modality 3D sub-diffraction resolution fluorescence and refractive-index reconstruction. *Biomed. Opt. Express* **8**, 5776–5793 (2017).

137. Shin, S., Kim, D., Kim, K. & Park, Y. Super-resolution three-dimensional fluorescence and optical diffraction tomography of live cells using structured illumination generated by a digital micromirror device. *Sci. Rep.* **8**, 9183 (2018).

138. Guo, R., Barnea, I. & Shaked, N. T. Limited-angle tomographic phase microscopy utilizing confocal scanning fluorescence microscopy. *Biomed. Opt. Express* **12**, 1869–1881 (2021).

139. Paidi, S. K. et al. Coarse Raman and optical diffraction tomographic imaging enable label-free phenotyping of isogenic breast cancer cells of varying metastatic potential. *Biosens. Bioelectron.* **175**, 112863 (2021).

140. Hsieh, C.-M. et al. Regulation of lipid droplets in live preadipocytes using optical diffraction tomography and Raman spectroscopy. *Opt. Express* **27**, 22994–23008 (2019).

141. Oh, S. et al. Protein and lipid mass concentration measurement in tissues by stimulated Raman scattering microscopy. *Proc. Natl Acad. Sci. USA* **119**, e2117938119 (2022).

142. Bailey, M. et al. Predicting the refractive index of tissue models using light scattering spectroscopy. *Appl. Spectrosc.* **75**, 574–580 (2021).

143. Scarcelli, G. et al. Noncontact three-dimensional mapping of intracellular hydromechanical properties by Brillouin microscopy. *Nat. Methods* **12**, 1132–1134 (2015).

144. Schlüßler, R. et al. Mechanical mapping of spinal cord growth and repair in living zebrafish larvae by Brillouin imaging. *Biophys. J.* **115**, 911–923 (2018).

145. Hauck, N. et al. PNIPAAm microgels with defined network architecture as temperature sensors in optical stretchers. *Mater. Adv.* **3**, 6179–6190 (2022).

146. Schlüßler, R. et al. Correlative all-optical quantification of mass density and mechanics of subcellular compartments with fluorescence specificity. *eLife* **11**, e68490 (2022).

147. Abuhattum, S. et al. Adipose cells and tissues soften with lipid accumulation while in diabetes adipose tissue stiffens. *Sci. Rep.* **12**, 1–17 (2022).

148. Kolb, J. et al. Small leucine-rich proteoglycans inhibit CNS regeneration by modifying the structural and mechanical properties of the lesion environment. Preprint at *bioRxiv* https://doi.org/10.1038/s41467-023-42339-7 AQ15 (2022).

149. Youle, R. J. & Van Der Bliek, A. M. Mitochondrial fission, fusion, and stress. *Science* **337**, 1062–1065 (2012).

150. Meyer, P. & Dworkin, J. Applications of fluorescence microscopy to single bacterial cells. *Res. Microbiol.* **158**, 187–194 (2007).

151. Costerton, J. The role of electron microscopy in the elucidation of bacterial structure and function. *Annu. Rev. Microbiol.* **33**, 459–479 (1979).

152. Joyner, R. P. et al. A glucose-starvation response regulates the diffusion of macromolecules. *eLife* **5**, e09376 (2016).

153. Rappaz, B. et al. Noninvasive characterization of the fission yeast cell cycle by monitoring dry mass with digital holographic microscopy. *J. Biomed. Opt.* **14**, 034049 (2009).

154. Odermatt, P. D. et al. Variations of intracellular density during the cell cycle arise from tip-growth regulation in fission yeast. *eLife* **10**, e64901 (2021).

155. Randazzo, A. et al. Optimal turnaround time for direct identification of microorganisms by mass spectrometry in blood culture. *J. Microbiol. Methods* **130**, 1–5 (2016).

156. Mukherjee, A. & Koller, M. Polyhydroxyalkanoate (PHA) biopolyesters — emerging and major products of industrial biotechnology. *EuroBiotech. J.* **6**, 49–60 (2022).

157. Peters, V. & Rehm, B. H. In vivo monitoring of PHA granule formation using GFP-labeled PHA synthases. *FEMS Microbiol. Lett.* **248**, 93–100 (2005).

158. Tian, J., Sinskey, A. J. & Stubbe, J. Kinetic studies of polyhydroxybutyrate granule formation in *Wautersia eutropha* H16 by transmi ssion electron microscopy. *J. Bacteriol.* **187**, 3814–3824 (2005).

159. Park, H. et al. Measuring cell surface area and deformability of individual human red blood cells over blood storage using quantitati ve phase imaging. *Sci. Rep.* **6**, 34257 (2016).

160. Kim, G., Jo, Y., Cho, H., Min, H.-S. & Park, Y. Learning-based screening of hematologic disorders using quantitative phase imaging of individual red blood cells. *Biosens. Bioelectron.* **123**, 69–76 (2019).

161. Yoon, J. et al. Identification of non-activated lymphocytes using three-dimensional refractive index tomography and machine learnin g. *Sci. Rep.* **7**, 6654 (2017).

162. Lee, S., Jang, S. & Park, Y. Measuring three-dimensional dynamics of platelet activation using 3-D quantitative phase imaging. Prep rint at *bioRxiv* https://doi.org/10.1101/827436 AQ16 (2019).

163. Stanly, T. A. et al. Quantitative optical diffraction tomography imaging of mouse platelets. *Front. Physiol.* **11**, 568087 (2020).

164. Mathiowetz, A. J. & Olzmann, J. A. Lipid droplets and cellular lipid flux. *Nat. Cell Biol*. https://doi.org/10.1038/s41556-024-01364-4 (2024).

165. Fam, T. K., Klymchenko, A. S. & Collot, M. Recent advances in fluorescent probes for lipid droplets. *Materials* **11**, 1768 (2018).

166. Kähärä, I. et al. Phototoxicity of BODIPY in long-term imaging can be reduced by intramolecular motion. *Photochem. Photobiol. Sc i.* **21**, 1677–1687 (2022).

167. Bumpus, T. W. & Baskin, J. M. Clickable substrate mimics enable imaging of phospholipase D activity. *ACS Cent. Sci.* **3**, 1070–1077 (2017).

168. Sandoz, P. A. et al. Label free 3D analysis of organelles in living cells by refractive index shows pre-mitotic organelle spinning in m ammalian stem cells. Preprint at *bioRxiv* https://doi.org/10.1101/407239 AQ17 (2018).

169. Silva, L. M. et al. *Besnoitia besnoiti* infection alters both endogenous cholesterol de novo synthesis and exogenous LDL uptake in h ost endothelial cells. *Sci. Rep.* **9**, 6650 (2019).

170. Park, S. et al. Label-free tomographic imaging of lipid droplets in foam cells for machine-learning-assisted therapeutic evaluation of targeted nanodrugs. *ACS Nano* **14**, 1856–1865 (2020).

171. Nuiyen, A. et al. Lack of Nck1 protein and Nck–CD3 interaction caused the increment of lipid content in Jurkat T cells. *BMC Mol. C ell Biol.* **23**, 1–14 (2022).

172. Brangwynne, C. P. et al. Germline P granules are liquid droplets that localize by controlled dissolution/condensation. *Science* **324**, 1 729–1732 (2009).

173. Li, P. et al. Phase transitions in the assembly of multivalent signalling proteins. *Nature* **483**, 336–340 (2012).

174. Lyon, A. S., Peeples, W. B. & Rosen, M. K. A framework for understanding the functions of biomolecular condensates across scales. *Nat. Rev. Mol. Cell Biol.* **22**, 215–235 (2021).

175. Boija, A., Klein, I. A. & Young, R. A. Biomolecular condensates and cancer. *Cancer Cell* **39**, 174–192 (2021).

176. Mathieu, C., Pappu, R. V. & Taylor, J. P. Beyond aggregation: pathological phase transitions in neurodegenerative disease. *Science* **3 70**, 56–60 (2020).

177. Kim, T. et al. RNA-mediated demixing transition of low-density condensates. *Nat. Commun.* **14**, 2425 (2023).

178. Posey, A. E., Holehouse, A. S. & Pappu, R. V. *Methods in Enzymology* Vol. 611, 1–30 (Elsevier, 2018).

179. Hong, Y. et al. Label-free quantitative analysis of coacervates via 3D phase imaging. *Adv. Opt. Mater.* **9**, 2100697 (2021).

180. McCall, P. et al. Label-free composition determination for biomolecular condensates with an arbitrarily large number of components AQ18 (2023).

181. Guillén-Boixet, J. et al. RNA-induced conformational switching and clustering of G3BP drive stress granule assembly by condensation. *Cell* **181**, 346–361.e17 (2020).

182. Qian, X. et al. Generation of human brain region-specific organoids using a miniaturized spinning bioreactor. *Nat. Protoc.* **13**, 565–580 (2018).

183. Yoon, K.-J. et al. Zika-virus-encoded NS2A disrupts mammalian cortical neurogenesis by degrading adherens junction proteins. *Cell Stem Cell* **21**, 349–358.e6 (2017).

184. Nishimura, K. et al. Live-cell imaging of subcellular structures for quantitative evaluation of pluripotent stem cells. *Sci. Rep.* **9**, 1777 (2019).

185. Orozco-Fuentes, S. et al. Quantification of the morphological characteristics of hESC colonies. *Sci. Rep.* **9**, 17569 (2019).

186. Wakui, T. et al. Method for evaluation of human induced pluripotent stem cell quality using image analysis based on the biological morphology of cells. *J. Med. Imaging* **4**, 044003 (2017).

187. Jiang, H. et al. Reconstruction of bovine spermatozoa substances distribution and morphological differences between Holstein and Korean native cattle using three-dimensional refractive index tomography. *Sci. Rep.* **9**, 8774 (2019).

188. Dardikman-Yoffe, G., Mirsky, S. K., Barnea, I. & Shaked, N. T. High-resolution 4-D acquisition of freely swimming human sperm cells without staining. *Sci. Adv.* **6**, eaay7619 (2020).

189. Chowdhury, S. et al. High-resolution 3D refractive index microscopy of multiple-scattering samples from intensity images. *Optica* **6**, 1211–1219 (2019).

190. Kim, J., Koo, B.-K. & Knoblich, J. A. Human organoids: model systems for human biology and medicine. *Nat. Rev. Mol. Cell Biol.* **21**, 571–584 (2020).

191. Stępień, P. et al. Numerical refractive index correction for the stitching procedure in tomographic quantitative phase imaging. *Biomed. Opt. Express* **13**, 5709–5720 (2022).

192. Yang, F. et al. Robust phase unwrapping via deep image prior for quantitative phase imaging. *IEEE Trans. Image Process.* **30**, 7025–7037 (2021).

193. Park, D. et al. Cryobiopsy: a breakthrough strategy for clinical utilization of lung cancer organoids. *Cells* **12**, 1854 (2023).

194. Artegiani, B. et al. Fast and efficient generation of knock-in human organoids using homology-independent CRISPR–Cas9 precision genome editing. *Nat. Cell Biol.* **22**, 321–331 (2020).

195. Roshanzadeh, A. et al. Surface charge-dependent cytotoxicity of plastic nanoparticles in alveolar cells under cyclic stretches. *Nano Lett.* **20**, 7168–7176 (2020).

196. Larrazabal, C., Hermosilla, C., Taubert, A. & Conejeros, I. 3D holotomographic monitoring of Ca^{++} dynamics during ionophore-induced *Neospora caninum* tachyzoite egress from primary bovine host endothelial cells. *Parasitol. Res.* **121**, 1169–1177 (2021).

197. Balk, M. et al. Cellular SPION uptake and toxicity in various head and neck cancer cell lines. *Nanomaterials* **11**, 726 (2021).

198. Kim, E. H. et al. Self-luminescent photodynamic therapy using breast cancer targeted proteins. *Sci. Adv.* **6**, eaba3009 (2020).

199. Park, S. et al. Detection of intracellular monosodium urate crystals in gout synovial fluid using optical diffraction tomography. *Sci. Rep.* **11**, 10019 (2021).

200. Sohn, M., Lee, J. E., Ahn, M., Park, Y. & Lim, S. Correlation of dynamic membrane fluctuations in red blood cells with diabetes mellitus and cardiovascular risks. *Sci. Rep.* **11**, 1–10 (2021).

201. Ziemczonok, M., Kuś, A., Wasylczyk, P. & Kujawińska, M. 3D-printed biological cell phantom for testing 3D quantitative phase imaging systems. *Sci. Rep.* **9**, 18872 (2019).

202. Park, Y. et al. Refractive index maps and membrane dynamics of human red blood cells parasitized by *Plasmodium falciparum*. *Proc. Natl Acad. Sci. USA* **105**, 13730–13735 (2008).

203. Kim, G. et al. Measurements of three-dimensional refractive index tomography and membrane deformability of live erythrocytes from *Pelophylax nigromaculatus*. *Sci. Rep.* **8**, 9192 (2018).

204. Choi, I., Lee, K. & Park, Y. Compensation of aberration in quantitative phase imaging using lateral shifting and spiral phase integration. *Opt. Express* **25**, 30771–30779 (2017).

205. Ryu, D. et al. Deep learning-based optical field screening for robust optical diffraction tomography. *Sci. Rep.* **9**, 15239 (2019).

206. Choi, G. et al. Cycle-consistent deep learning approach to coherent noise reduction in optical diffraction tomography. *Opt. Express* **27**, 4927–4943 (2019).

207. Wang, Z. et al. Spatial light interference microscopy (SLIM). *Opt. Express* **19**, 1016–1026 (2011).

208. Charrière, F. et al. Shot-noise influence on the reconstructed phase image signal-to-noise ratio in digital holographic microscopy. *Appl. Opt.* **45**, 7667–7673 (2006).

209. Ghiglia, D. C. & Romero, L. A. Minimum Lp-norm two-dimensional phase unwrapping. *J. Opt. Soc. Am. A* **13**, 1999–2013 (1996).

210. Lee, D. et al. High-fidelity optical diffraction tomography of live organisms using iodixanol refractive index matching. *Biomed. Opt. Express* **13**, 6404–6415 (2022).

211. Kostencka, J., Kozacki, T., Kuś, A., Kemper, B. & Kujawińska, M. Holographic tomography with scanning of illumination: space-domain reconstruction for spatially invariant accuracy. *Biomed. Opt. Express* **7**, 4086–4101 (2016).

212. Chung, Y. et al. Label-free histological analysis of retrieved thrombi in acute ischemic stroke using optical diffraction tomography and deep learning. Preprint at *bioRxiv* https://doi.org/10.1101/2023.02.22.529519 AQ19 (2023).

213. Zheng, Y. et al. A graph-transformer for whole slide image classification. *IEEE Trans. Med. Imaging* **41**, 3003–3015 (2022).

214. Lee, Y. et al. Derivation of prognostic contextual histopathological features from whole-slide images of tumours via graph deep learning. *Nat. Biomed. Eng*. https://doi.org/10.1038/s41551-022-00923-0 (2022).

215. Schelkens, P. et al. Compression strategies for digital holograms in biomedical and multimedia applications. *Light Adv. Manuf.* **3**, 601–621 (2022).

216. Lim, J., Ayoub, A. B. & Psaltis, D. Three-dimensional tomography of red blood cells using deep learning. *Adv. Photon.* **2**, 026001 (2020).

217. Ryu, D. et al. Label-free white blood cell classification using refractive index tomography and deep learning. *BME Front.* **2021**, 9893804 (2021).

218. Hassaan, M. et al. Breast cancer diagnosis using spatial light interference microscopy. *J. Biomed. Opt.* **20**, 111210 (2015).

219. Tu, H. et al. Stain-free histopathology by programmable supercontinuum pulses. *Nat. Photon.* **10**, 534–540 (2016).

220. Lee, M. et al. Label-free optical quantification of structural alterations in Alzheimer's disease. *Sci. Rep.* **6**, 31034 (2016).

221. Zhuo, W., Gabriel, P., Krishnarao, V. T. & Andre, B. Tissue refractive index as marker of disease. *J. Biomed. Opt.* **16**, 116017 (2011).

222. Rivenson, Y. et al. PhaseStain: the digital staining of label-free quantitative phase microscopy images using deep learning. *Light Sci. Appl.* **8**, 23 (2019).

223. Costantini, I., Cicchi, R., Silvestri, L., Vanzi, F. & Pavone, F. S. In-vivo and ex-vivo optical clearing methods for biological tissues. *Biomed. Opt. Express* **10**, 5251–5267 (2019).

224. Kandel, M. E. et al. Reproductive outcomes predicted by phase imaging with computational specificity of spermatozoon ultrastructure. *Proc. Natl Acad. Sci. USA* **117**, 18302–18309 (2020).

225. Herrero, J. & Meseguer, M. Selection of high potential embryos using time-lapse imaging: the era of morphokinetics. *Fertil. Steril.* **99**, 1030–1034 (2013).

226. Dimitriadis, I., Zaninovic, N., Badiola, A. C. & Bormann, C. L. Artificial intelligence in the embryology laboratory: a review. *Reprod. BioMedicine Online* **44**, 435–448 (2022).

227. Barnes, J. et al. A non-invasive artificial intelligence approach for the prediction of human blastocyst ploidy: a retrospective model development and validation study. *Lancet Digital Health* **5**, e28–e40 (2023).